ANZIAM J. 56(2015), 317–358
doi:10.1017/S1446181115000085

KELVIN–HELMHOLTZ CREEPING FLOW AT THE INTERFACE BETWEEN TWO VISCOUS FLUIDS

LAWRENCE K. FORBES[✉1], RHYS A. PAUL[1], MICHAEL J. CHEN[1,2] and DAVID E. HORSLEY[1]

(Received 18 October, 2013; revised 18 March, 2015)

Abstract

The Kelvin–Helmholtz flow is a shearing instability that occurs at the interface between two fluids moving with different speeds. Here, the two fluids are each of finite depth, but are highly viscous. Consequently, their motion is caused by the horizontal speeds of the two walls above and below each fluid layer. The motion of the fluids is assumed to be governed by the Stokes approximation for slow viscous flow, and the fluid motion is thus responsible for movement of the interface between them. A linearized solution is presented, from which the decay rate and the group speed of the wave system may be obtained. The nonlinear equations are solved using a novel spectral representation for the streamfunctions in each of the two fluid layers, and the exact boundary conditions are applied at the unknown interface location. Results are presented for the wave profiles, and the behaviour of the curvature of the interface is discussed. These results are compared to the Boussinesq–Stokes approximation which is also solved by a novel spectral technique, and agreement between the results supports the numerical calculations.

2010 *Mathematics subject classification*: primary 76D07; secondary 76D33.

Keywords and phrases: curvature singularity, Kelvin–Helmholtz instability, interface, spectral representation, Stokes flow.

1. Introduction

Kelvin–Helmholtz flow is a classical problem of fluid mechanics. Traditionally, it occurs when two inviscid fluids, subject to the downward acceleration of gravity, flow past each other in horizontal layers and with different speeds. The interface between the fluids is then subject to shearing instabilities, so that any small perturbation to an otherwise horizontal interface grows rapidly in time. If the disturbance is periodic in

[1]School of Mathematics and Physics, University of Tasmania, Private Bag 37, Hobart, Tasmania, Australia; e-mail: Larry.Forbes@utas.edu.au, Rhys.Paul@utas.edu.au, David.Horsley@utas.edu.au.
[2]Department of Applied Mathematics, University of Adelaide, South Australia 5005, Australia; e-mail: michael.chen@adelaide.edu.au.

the horizontal direction, then it may be expressed as a Fourier series in space with time-dependent coefficients, and it is well known that higher Fourier modes grow with time more rapidly than the lower ones. This is discussed in detail in the texts by Chandrasekhar [5, p. 485] and Drazin and Reid [8]. This classical analysis is based on a linearization of the equations of inviscid fluid mechanics, and assumes that the disturbance to the interface remains small.

Linearized theory predicts that disturbances grow exponentially rapidly with time, with a growth rate dependent on the difference in the two horizontal fluid speeds. Such a rapid growth in the amplitude of the disturbance must eventually violate the small-amplitude assumption on which linearization is predicated, so that nonlinear effects become important in a finite time. Thus, a disturbance that starts out as a pure sinusoid does not remain so for long, and may develop overhanging portions resembling breaking waves. After some time, the interface can roll up into the famous *cat's eyes* spirals as illustrated in the album by Van Dyke [27, p. 85].

Since linear theory indicates that the higher Fourier modes grow most rapidly, it is perhaps to be expected that the Fourier series for *derivatives* of the interface shape may fail to converge within finite time. Indeed, Moore [20] presented an asymptotic analysis for inviscid fluids that showed how the curvature of the interface becomes infinite at a certain point, and estimated the critical time needed for this to occur. Cowley et al. [7] also carried out an asymptotic study of the curvature singularity at the interface in the Kelvin–Helmholtz flow. In their approach, time was considered as a complex variable, and curvature singularities in the complex plane eventually moved onto the real time axis at a finite value, so confirming Moore's prediction of a finite-time singularity in the interfacial curvature.

In view of these observations, it is not surprising that the numerical computation of the highly nonlinear interfacial shapes formed in the Kelvin–Helmholtz problem is a difficult undertaking, at least with inviscid fluids. Numerical solutions of the inviscid equations produce a periodic disturbance that grows for a time, but the algorithm then fails, at a time slightly less than the critical time at which Moore [20] predicted a curvature singularity. To overcome this, Krasny [17] introduced a type of *vortex blob* method, in which the interface is effectively replaced with an interfacial zone of finite width. He was able to continue the calculations beyond Moore's critical time, and did indeed achieve an interface that rolled up into spiral formations. In some sense, this is believed to mimic the effects of the viscosity that would be encountered in a real fluid, damping the curvature singularity and preventing its occurrence. Nevertheless, Baker and Pham [2] subsequently demonstrated that different types of *vortex blob* methods would produce somewhat different numerical interface behaviours, so that the computed flow is not entirely independent of the numerical solution technique. In spite of this, however, Tryggvason et al. [26] demonstrated that *vortex blob* approaches can be made to agree fairly well with the results of full viscous simulation.

The role played by viscosity at the interface is subtle and intriguing. When the fluids are miscible, the curvature singularity at the interface predicted by inviscid

https://doi.org/10.1017/S1446181115000085 Published online by Cambridge University Press

theory is replaced with a small patch of high vorticity, and this is responsible for the interface turning over to form overhanging segments. This was demonstrated explicitly by Forbes [11] in a numerical solution of the Rayleigh–Taylor instability, in which a heavier fluid lay above a less dense one. In that problem, it was found that the vorticity was essentially zero nearly everywhere, except at the precise times and places at which the inviscid model predicted a curvature singularity, where there was instead a small intense region of high vorticity. A similar conclusion was obtained by Chen and Forbes [6] for the Kelvin–Helmholtz instability in miscible fluids. Those authors first solved the inviscid problem, using a smoothing algorithm to control the growth of the higher Fourier modes in their solution, and monitored the locations of the maximum and minimum curvatures at the interface for different times. These two locations become closer as time progresses, eventually coalescing to form the curvature singularity in the inviscid case. In their viscous solution, this was the time and location of the small intense patch of vorticity that caused the overturning of the interface. Tauber et al. [25] studied the viscous planar Kelvin–Helmholtz problem, but for the immiscible case in which there was a sharp interface separating two fluids of different densities and viscosities. Their finite-difference technique produced interfaces with long fingers of fluid penetrating into the other layer, in cases when the surface tension was large. Similar long fingers were obtained by Li et al. [19] for fluids of equal density and with zero gravity, and Shadloo and Yildiz [23] observed similar profiles for large density differences, using a smooth-particle hydrodynamics code.

The inviscid problem represents one extreme of modelling for the Kelvin–Helmholtz problem, and ignores the effects of fluid viscosity altogether. The opposite case is the Stokes flow approximation [22], in which each of the two fluids is considered to be so viscous that the inertial and convective terms in the Navier–Stokes momentum equations may be disregarded. The motion of each fluid is then governed by the Stokes equations and the incompressibility condition. This is a linear system of partial differential equations and, therefore, as in the purely inviscid case, exact forms of the solution variables can be written down for each fluid. However, the problem is nonlinear overall, since the location of the interface is unknown *a priori*. The problem has been considered by Pozrikidis [22], who used an integral-equation formulation with a Green function to satisfy the equations in each fluid exactly. This leads to an equation to be solved at the interface only, and this is integrated forward in time. Results were presented for equal fluid densities and long fingers of interpenetrating fluids were observed at the interface.

Since the field equations in the case of Stokes flow are linear, spectral methods may also be brought to bear on this problem. They offer the possible advantages that they are computationally fast and permit difficult quantities, such as curvature of the interface, to be calculated with high accuracy, since exact differentiation of the assumed form of the solution is possible. In addition, spectral techniques can ensure conservation of key quantities such as mass over long times, in a manner that is not

https://doi.org/10.1017/S1446181115000085 Published online by Cambridge University Press

always easy to ensure in other numerical techniques. Forbes et al. [13] developed a novel spectral method for solving interfacial flow problems in purely inviscid fluids and, since then, the technique has been used successfully in a variety of applications, such as a study of the Faraday oscillations in vertically shaken containers of fluid [16]. Somewhat similar spectral methods have also been used by Faltinsen and Timokha [10], but the one proposed by Forbes et al. [13] additionally derives certain identities between quantities at the interface, so that an accurate solution may be obtained only using standard integration routines.

A key aim of the present paper is to extend the spectral method of Forbes et al. [13] to the case of creeping viscous flows with an interface, in which the flow of each fluid is described by the Stokes equation. The governing equations are outlined in Section 2, and the full linearized solution is given in Section 3. The new spectral method is developed in Section 4 for the nonlinear problem, and the results of computation are presented in Section 5. We have found that even for highly viscous flows, ignoring the nonlinear convection terms in the governing equations (as is the case in the Stokes approximation) still allows curvature singularities to develop at the interface. This is controlled here by a very sparse use of Lanczos smoothing [15]. As a comparison, a Boussinesq approximation to this Stokes flow problem is developed in Section 6. Here, the exact interface is replaced by an approximate zone in which the density varies smoothly from one fluid region to the other, and a new spectral method is used to solve this problem. It now permits the interfacial zone to form overhanging sections, since it is no longer limited by a curvature singularity; instead, portions of high vorticity are formed near the overhanging regions. The agreement between these approximate results and those of the full problem in Section 5, at least at early times, lends strong support to the viability of the results. A summary and discussion in Section 7 concludes the paper.

2. The Stokes-flow model

Consider a system of two incompressible viscous fluids, separated by a sharp horizontal interface lying along the x-axis of a Cartesian coordinate system. Upper fluid 2 has constant density ρ_2 and is bounded above by a rigid wall at height $y = H_2$. Lower fluid 1 has density ρ_1 and lies in the vertical layer $-H_1 < y < 0$. The upper wall moves horizontally with some speed c_2, and the bottom wall at $y = -H_1$ moves at speed c_1. An initial periodic disturbance is now made to the system, such that the interface between the fluids adopts some periodic profile, $y = \eta(x, t)$, with wavelength λ and initial amplitude ϵ. In the Stokes-flow hypothesis [22], the inertial and convective terms in the Navier–Stokes equations of viscous fluid flow are considered small, so that

$$\frac{1}{\rho_j}\nabla p_j = -g\mathbf{j} + \nu_j \nabla^2 \mathbf{q}_j \tag{2.1}$$

becomes the governing momentum equation in each fluid layer $j = 1, 2$. Here, g is the downward acceleration of gravity in the negative y-direction and $\mathbf{j}$ denotes the

https://doi.org/10.1017/S1446181115000085 Published online by Cambridge University Press

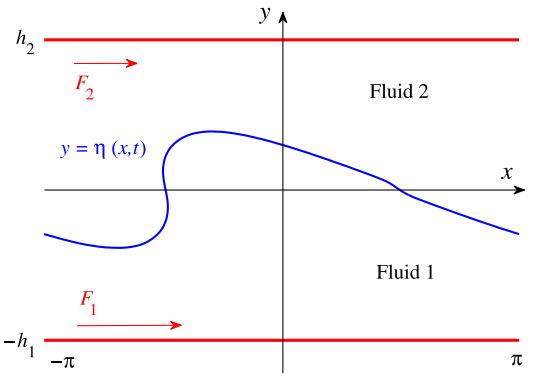

FIGURE 1. A sketch of the dimensionless flow problem for the viscous Kelvin–Helmholtz problem. The interface is taken from an actual solution with $D = 0.97$, $F_1 = 0.1$, $F_2 = -0.1$, $R_1 = R_2 = 1$, $h_1 = h_2 = 1$ and surface-tension parameter $\sigma = 0.008$. The initial perturbation was sinusoidal with amplitude $\epsilon = 0.4$, and the nonlinear solution is shown at time $t = 24$.

unit vector up the vertical y-axis. The pressures are p_j and the velocity vectors are represented as $\mathbf{q}_j = u_j\mathbf{i} + v_j\mathbf{j}$, where u_j and v_j are the components in the horizontal and vertical directions, respectively. The viscosities in the two layers are ν_j for $j = 1, 2$.

At this point, dimensionless variables are introduced, which will be used throughout the remainder of the paper. The length scale is chosen to be $\lambda/(2\pi)$ based on the wavelength λ of the periodic disturbance, and an appropriate scale for speed is $\sqrt{\lambda g/(2\pi)}$. The time is therefore nondimensionalized by reference to the quantity $\sqrt{\lambda/(2\pi g)}$. The densities are referenced to the density ρ_1 of the fluid in lower layer 1, and the scale for pressure is then $\rho_1 g\lambda/(2\pi)$. A sketch of the dimensionless problem is presented in Figure 1.

The solution is, therefore, dependent on the eight dimensionless parameters

$$D = \frac{\rho_2}{\rho_1}, \quad F_j = c_j\sqrt{\frac{2\pi}{g\lambda}}, \quad R_j = \nu_j\frac{2\pi}{\lambda}\sqrt{\frac{2\pi}{g\lambda}},$$
$$h_j = \frac{2\pi H_j}{\lambda}, \quad j = 1, 2.$$

The first of these is the density ratio of the upper to the lower fluids and, for Kelvin–Helmholtz flow, $D < 1$. The next two quantities F_1 and F_2 are Froude numbers in the two fluid layers, and give a measure of the dimensionless horizontal flow speed at the lower and upper walls, respectively. The two constants R_1 and R_2 may be thought of as inverse Reynolds numbers in each fluid layer, and they represent the dimensionless viscosity of each fluid; for Stokes flow, R_1 and R_2 are considered to be large. The dimensionless depths of the lower and upper fluid layers are h_1 and h_2, respectively. Finally, provision is made in this study for the inclusion of surface tension, and this will be represented by the dimensionless coefficient σ.

https://doi.org/10.1017/S1446181115000085 Published online by Cambridge University Press

In each fluid, the incompressibility conditions are expressed as

$$\frac{\partial u_j}{\partial x} + \frac{\partial v_j}{\partial y} = 0, \quad j = 1, 2 \tag{2.2}$$

with u_j and v_j denoting the horizontal and vertical components of the two fluid velocity vectors, respectively. In the lower fluid 1, the two components of the Stokes momentum equation (2.1) in dimensionless form are

$$\frac{\partial p_1}{\partial x} = R_1 \nabla^2 u_1, \quad \frac{\partial p_1}{\partial y} = -1 + R_1 \nabla^2 v_1, \quad -h_1 < y < \eta(x,t) \tag{2.3}$$

and, in the upper fluid 2, the Stokes equations become

$$\frac{1}{D}\frac{\partial p_2}{\partial x} = R_2 \nabla^2 u_2, \quad \frac{1}{D}\frac{\partial p_2}{\partial y} = -1 + R_2 \nabla^2 v_2, \quad \eta(x,t) < y < h_2. \tag{2.4}$$

Here, $y = \eta(x,t)$ is the equation for the location of the interface between the fluids.

Each fluid must obey the kinematic condition that it is not free to cross its own interface. This leads to the two boundary conditions

$$v_j = \frac{\partial \eta}{\partial t} + u_j \frac{\partial \eta}{\partial x}, \quad j = 1, 2, \text{ on } y = \eta(x,t). \tag{2.5}$$

Since the two fluids are both viscous, the no-slip boundary condition at the interface also requires the continuity of both the horizontal and vertical velocity components, so that

$$u_1 = u_2, \quad v_1 = v_2 \quad \text{on } y = \eta(x,t). \tag{2.6}$$

For viscous fluids, there is also a vector dynamic boundary condition at the interface, which requires the continuity of both the tangential and normal stress components. Further details are given in Batchelor [4, p. 150]. The tangential dynamic condition takes the form

$$\begin{aligned} DR_2\left[\left(\frac{\partial v_2}{\partial y} - \frac{\partial u_2}{\partial x}\right)\eta_x + \frac{1}{2}\left(\frac{\partial u_2}{\partial y} + \frac{\partial v_2}{\partial x}\right)(1 - \eta_x^2)\right] \\ = R_1\left[\left(\frac{\partial v_1}{\partial y} - \frac{\partial u_1}{\partial x}\right)\eta_x + \frac{1}{2}\left(\frac{\partial u_1}{\partial y} + \frac{\partial v_1}{\partial x}\right)(1 - \eta_x^2)\right] \end{aligned} \tag{2.7}$$

on $y = \eta(x,t)$. The continuity of normal stress at the interface involves the fluid pressures, and becomes

$$\begin{aligned} p_2(1 + \eta_x^2) - 2DR_2\left[\frac{\partial u_2}{\partial x}\eta_x^2 - \left(\frac{\partial u_2}{\partial y} + \frac{\partial v_2}{\partial x}\right)\eta_x + \frac{\partial v_2}{\partial y}\right] \\ = p_1(1 + \eta_x^2) - 2R_1\left[\frac{\partial u_1}{\partial x}\eta_x^2 - \left(\frac{\partial u_1}{\partial y} + \frac{\partial v_1}{\partial x}\right)\eta_x + \frac{\partial v_1}{\partial y}\right] \\ + \sigma\frac{\eta_{xx}}{[1 + \eta_x^2]^{1/2}} \quad \text{on } y = \eta(x,t). \end{aligned} \tag{2.8}$$

https://doi.org/10.1017/S1446181115000085 Published online by Cambridge University Press

The last term in equation (2.8) corresponds to the effects of surface tension on the interface.

The two incompressibility conditions (2.2) may now be satisfied identically by making use of streamfunctions ψ_1 and ψ_2 in the lower and upper fluids, respectively. In each fluid,

$$u_j = \frac{\partial \psi_j}{\partial y}, \quad v_j = -\frac{\partial \psi_j}{\partial x}, \quad j = 1, 2 \tag{2.9}$$

as discussed in Batchelor [4, p. 76]. Substituting these relations (2.9) into the Stokes equations (2.3) and (2.4) yields the well-known biharmonic equations

$$\nabla^4 \psi_j = \frac{\partial^4 \psi_j}{\partial x^4} + 2\frac{\partial^4 \psi_j}{\partial x^2 \partial y^2} + \frac{\partial^4 \psi_j}{\partial y^4} = 0, \quad j = 1, 2. \tag{2.10}$$

A discussion of these equations is given by Ockendon and Ockendon [21, p. 55].

To begin, it is necessary to consider an exact solution of these governing equations (2.10) and boundary conditions (2.5)–(2.8), in the case of purely horizontal flow in which $\eta(x, t) = 0$. After a little algebra, it is evident that the appropriate horizontal flows are given by the choices

$$\begin{aligned} \psi_1(y) &= F_1 y + \frac{DR_2(F_2 - F_1)}{2(h_2 R_1 + h_1 DR_2)}(y + h_1)^2, \\ \psi_2(y) &= F_2 y + \frac{R_1(F_2 - F_1)}{2(h_2 R_1 + h_1 DR_2)}(y - h_2)^2. \end{aligned} \tag{2.11}$$

The first streamfunction ψ_1 in this system (2.11) satisfies the requirement that $u_1 = F_1$ and $v_1 = 0$ at the lower wall $y = -h_1$, with the two velocity components obtained from equation (2.9), and the second streamfunction similarly satisfies $u_2 = F_2$ and $v_2 = 0$ at the upper wall $y = h_2$. On the horizontal interface $\eta = 0$, the two functions in (2.11) obey the no-slip conditions (2.6) and the tangential dynamic condition (2.7), and each is a solution of the biharmonic equations in the system (2.10).

It is now possible to construct the full spectral representation for the streamfunctions in each of the two fluid layers, assuming a solution that is 2π-periodic in the horizontal coordinate x. In the lower fluid 1, the required form satisfying the biharmonic equation (2.10) is

$$\begin{aligned} \psi_1(x, y, t) = F_1 y &+ \frac{DR_2(F_2 - F_1)}{2(h_2 R_1 + h_1 DR_2)}(y + h_1)^2 \\ &+ \sum_{n=1}^{N} [A_{1n}(t) Z_{1n}(y) + C_{1n}(t) Z_{2n}(y)] \cos(nx) \\ &+ [B_{1n}(t) Z_{1n}(y) + D_{1n}(t) Z_{2n}(y)] \sin(nx), \end{aligned} \tag{2.12}$$

while the corresponding streamfunction in the upper fluid 2 is written as

https://doi.org/10.1017/S1446181115000085 Published online by Cambridge University Press

$$\psi_2(x,y,t) = F_2 y + \frac{R_1(F_2-F_1)}{2(h_2R_1+h_1DR_2)}(y-h_2)^2 + \sum_{n=1}^{N}[A_{2n}(t)Z_{3n}(y) + C_{2n}(t)Z_{4n}(y)]\cos(nx) + [B_{2n}(t)Z_{3n}(y) + D_{2n}(t)Z_{4n}(y)]\sin(nx). \tag{2.13}$$

In these two expressions, the four intermediate functions are defined to be

$$\begin{aligned} Z_{1n} &= \frac{\sinh(n(y+h_1)) - n(y+h_1)\cosh(n(y+h_1))}{\cosh(nh_1)}, \\ Z_{2n} &= \frac{n(y+h_1)\sinh(n(y+h_1))}{\cosh(nh_1)}, \\ Z_{3n} &= \frac{\sinh(n(y-h_2)) - n(y-h_2)\cosh(n(y-h_2))}{\cosh(nh_2)}, \\ Z_{4n} &= \frac{n(y-h_2)\sinh(n(y-h_2))}{\cosh(nh_2)}. \end{aligned} \tag{2.14}$$

These functions (2.14) are chosen to give periodic solutions to the two biharmonic equations (2.10), and the constants in the denominators are to ensure that the functions continue to take moderate values, even for large n and y, so that the determination of the unknown Fourier coefficients in the two series (2.12) and (2.13) remains a well-conditioned problem. In order to satisfy the requirements $u_1 = F_1$ and $v_1 = 0$ at the lower wall $y = -h_1$, the two conditions $Z_{1n}(-h_1) = Z_{2n}(-h_1) = 0$ and $Z'_{1n}(-h_1) = Z'_{2n}(-h_1) = 0$ have been imposed; similarly, $Z_{3n}(h_2) = Z_{4n}(h_2) = 0$ and $Z'_{3n}(h_2) = Z'_{4n}(h_2) = 0$ are stipulated at the upper wall $y = h_2$, so that the representation (2.13) satisfies $u_2 = F_2$ and $v_2 = 0$ there.

The velocity components in each fluid can be calculated from equation (2.9) using straightforward differentiation of the two series (2.12) and (2.13). A spectral representation for the pressure p_1 in the lower fluid is then obtained from equations (2.3) and, after some algebra, the result is

$$p_1(x,y,t) = -y + 2R_1\sum_{n=1}^{N} n^2[-A_{1n}(t)W_{1n}(y) + C_{1n}(t)W_{2n}(y)]\sin(nx) + n^2[B_{1n}(t)W_{1n}(y) - D_{1n}(t)W_{2n}(y)]\cos(nx). \tag{2.15}$$

Similarly, the Stokes equations (2.4) in the upper fluid can be solved to give the representation

$$p_2(x,y,t) = -Dy + 2DR_2\sum_{n=1}^{N} n^2[-A_{2n}(t)W_{3n}(y) + C_{2n}(t)W_{4n}(y)]\sin(nx) + n^2[B_{2n}(t)W_{3n}(y) - D_{2n}(t)W_{4n}(y)]\cos(nx) \tag{2.16}$$

for the pressure in that upper layer. The four intermediate functions in these expressions come from taking the appropriate derivatives of the quantities in the

https://doi.org/10.1017/S1446181115000085 Published online by Cambridge University Press

expressions (2.14), and are found to be

$$\begin{aligned} W_{1n} &= \frac{\cosh(n(y+h_1))}{\cosh(nh_1)}, \\ W_{2n} &= \frac{\sinh(n(y+h_1))}{\cosh(nh_1)}, \\ W_{3n} &= \frac{\cosh(n(y-h_2))}{\cosh(nh_2)}, \\ W_{4n} &= \frac{\sinh(n(y-h_2))}{\cosh(nh_2)}. \end{aligned} \tag{2.17}$$

It follows from the Stokes equations (2.3), (2.4) and the continuity equations (2.2) that the two pressures in equations (2.15) and (2.16) are solutions of Laplace's equation, and this is reflected in the forms of the functions in equations (2.17).

These expressions are essentially exact, at least in the limit $N \to \infty$, but, as yet, the eight sets of coefficient functions $A_{1n}(t)$, $A_{2n}(t)$ and so on remain unknown. They must be determined from the boundary conditions (2.5)–(2.8) at the interface.

3. The linearized solution

It is possible to develop a linearized solution to the governing equations in Section 2 using the initial perturbation amplitude ϵ as the small parameter. The appropriate expansions are

$$\begin{aligned} u_1(x,y,t) &= U_{10}(y) + \epsilon\tilde{U}_1(x,y,t) + O(\epsilon^2), \\ v_1(x,y,t) &= \epsilon\tilde{V}_1(x,y,t) + O(\epsilon^2), \\ u_2(x,y,t) &= U_{20}(y) + \epsilon\tilde{U}_2(x,y,t) + O(\epsilon^2), \\ v_2(x,y,t) &= \epsilon\tilde{V}_2(x,y,t) + O(\epsilon^2), \\ p_1(x,y,t) &= -y + \epsilon\tilde{P}_1(x,y,t) + O(\epsilon^2), \\ p_2(x,y,t) &= -Dy + \epsilon\tilde{P}_2(x,y,t) + O(\epsilon^2), \\ \eta(x,t) &= \epsilon\tilde{\eta}(x,t) + O(\epsilon^2). \end{aligned} \tag{3.1}$$

The zeroth-order horizontal velocity components

$$\begin{aligned} U_{10}(y) &= F_1 + \frac{DR_2(F_2-F_1)}{(h_2R_1 + h_1DR_2)}(y+h_1), \\ U_{20}(y) &= F_2 + \frac{R_1(F_2-F_1)}{(h_2R_1 + h_1DR_2)}(y-h_2) \end{aligned} \tag{3.2}$$

are obtained from differentiation of equations (2.11). For convenience, the surface tension will be ignored, so that $\sigma = 0$.

These expansions in (3.1) are now substituted into the boundary conditions at the interface, and only terms of first order in ϵ are retained. The first kinematic condition in the system (2.5) linearizes to become

$$\tilde{V}_1 = \tilde{\eta}_t + U_{10}(0)\tilde{\eta}_x \quad \text{on } y = 0, \tag{3.3}$$

https://doi.org/10.1017/S1446181115000085 Published online by Cambridge University Press

and the two no-slip conditions (2.6) yield

$$U'_{10}(0)\tilde{\eta} + \tilde{U}_1 = U'_{20}(0)\tilde{\eta} + \tilde{U}_2,$$
$$\tilde{V}_1 = \tilde{V}_2 \quad \text{on } y = 0. \tag{3.4}$$

The linearized form of the tangential dynamic condition (2.7) is

$$DR_2\left[\frac{\partial \tilde{U}_2}{\partial y} + \frac{\partial \tilde{V}_2}{\partial x}\right] = R_1\left[\frac{\partial \tilde{U}_1}{\partial y} + \frac{\partial \tilde{V}_1}{\partial x}\right] \quad \text{on } y = 0, \tag{3.5}$$

and the normal dynamic condition (2.8) yields

$$-D\tilde{\eta} + \tilde{P}_2 - 2DR_2\frac{\partial \tilde{V}_2}{\partial y} = -\tilde{\eta} + \tilde{P}_1 - 2R_1\frac{\partial \tilde{V}_1}{\partial y} \quad \text{on } y = 0. \tag{3.6}$$

The perturbation functions $\tilde{U}_1$, $\tilde{V}_1$ and so on have series forms that can be derived from equations (2.12)–(2.16). For example, the horizontal velocity components in each fluid can be obtained by differentiating the streamfunctions (2.12) and (2.13) as in equations (2.9). When they are evaluated at $y = 0$, as required in this linearized solution, we get

$$\begin{aligned}\tilde{U}_1(x,y,t) &= [\tilde{A}_{1n}(t)Z'_{1n}(y) + \tilde{C}_{1n}(t)Z'_{2n}(y)]\cos(nx)\\ &\quad + [\tilde{B}_{1n}(t)Z'_{1n}(y) + \tilde{D}_{1n}(t)Z'_{2n}(y)]\sin(nx),\\ \tilde{U}_2(x,y,t) &= [\tilde{A}_{2n}(t)Z'_{3n}(y) + \tilde{C}_{2n}(t)Z'_{4n}(y)]\cos(nx)\\ &\quad + [\tilde{B}_{2n}(t)Z'_{3n}(y) + \tilde{D}_{2n}(t)Z'_{4n}(y)]\sin(nx),\end{aligned}$$

and similarly for the other dependent variables. The perturbed interface elevation is represented as

$$\tilde{\eta}(x,t) = \tilde{G}_n(t)\cos(nx) + \tilde{H}_n(t)\sin(nx).$$

The linearized boundary conditions (3.3)–(3.6) have both an odd and an even component, and so they constitute a system of 10 equations for the 10 coefficient functions $\tilde{A}_{jn}$, $\tilde{B}_{jn}$, $\tilde{C}_{jn}$, $\tilde{D}_{jn}$, $j = 1, 2$, $\tilde{G}_n$ and $\tilde{H}_n$.

The two linearized no-slip conditions (3.4) give the relations

$$\begin{aligned}\tilde{A}_{2n}(t) &= \sigma_1\tilde{A}_{1n}(t) + \sigma_2\tilde{C}_{1n}(t) - \sigma_3\tilde{G}_n(t),\\ \tilde{B}_{2n}(t) &= \sigma_1\tilde{B}_{1n}(t) + \sigma_2\tilde{D}_{1n}(t) - \sigma_3\tilde{H}_n(t),\\ \tilde{C}_{2n}(t) &= \tau_1\tilde{A}_{1n}(t) + \tau_2\tilde{C}_{1n}(t) + \tau_3\tilde{G}_n(t),\\ \tilde{D}_{2n}(t) &= \tau_1\tilde{B}_{1n}(t) + \tau_2\tilde{D}_{1n}(t) + \tau_3\tilde{H}_n(t)\end{aligned} \tag{3.7}$$

between the unknown coefficients after considerable algebra. In these expressions, it is convenient to introduce additional constants

$$\begin{aligned}\sigma_1 &= \frac{Z_{1n}(0)Z'_{4n}(0) - Z'_{1n}(0)Z_{4n}(0)}{Z_{3n}(0)Z'_{4n}(0) - Z'_{3n}(0)Z_{4n}(0)},\\ \sigma_2 &= \frac{Z_{2n}(0)Z'_{4n}(0) - Z'_{2n}(0)Z_{4n}(0)}{Z_{3n}(0)Z'_{4n}(0) - Z'_{3n}(0)Z_{4n}(0)},\\ \sigma_3 &= \frac{Z_{4n}(0)[U'_{10}(0) - U'_{20}(0)]}{Z_{3n}(0)Z'_{4n}(0) - Z'_{3n}(0)Z_{4n}(0)},\end{aligned} \tag{3.8}$$

https://doi.org/10.1017/S1446181115000085 Published online by Cambridge University Press

in which the functions Z_{1n}, U_{10} and so on are as defined in equations (2.14) and (3.2). The remaining three constants τ_1, τ_2 and τ_3 are identical to these, except that every appearance of the function Z_{4n} in the numerators of the expressions in (3.8) must be replaced by Z_{3n}, while the denominators remain unchanged. The linearized tangential condition (3.5) yields the further two relations

$$\begin{aligned} \tilde{C}_{1n}(t) &= -\xi_1 \tilde{A}_{1n}(t) + \xi_2 \tilde{G}_n(t), \\ \tilde{D}_{1n}(t) &= -\xi_1 \tilde{B}_{1n}(t) + \xi_2 \tilde{H}_n(t), \end{aligned} \tag{3.9}$$

in which two additional constants

$$\begin{aligned} \xi_1 &= \frac{DR_2[nh_2\sigma_1 + \alpha_{n2}\tau_1] + R_1 nh_1}{DR_2[nh_2\sigma_2 + \alpha_{n2}\tau_2] - R_1\alpha_{n1}}, \\ \xi_2 &= \frac{DR_2[nh_2\sigma_3 - \alpha_{n2}\tau_3]}{DR_2[nh_2\sigma_2 + \alpha_{n2}\tau_2] - R_1\alpha_{n1}} \end{aligned} \tag{3.10}$$

have been introduced; these, in turn involve the constants

$$\begin{aligned} \alpha_{nj} &= 1 + nh_j \tanh(nh_j), \\ \beta_{nj} &= 1 - nh_j \tanh(nh_j), \quad j = 1, 2. \end{aligned}$$

The linearized normal dynamic condition (3.6) next yields a relation between the coefficients defining the two streamfunctions and those which describe the interface shape. These relations are

$$\begin{aligned} \eta_1 \tilde{A}_{1n}(t) &= \eta_2 \tilde{G}_n(t) - (1 - D)\tilde{H}_n(t), \\ \eta_1 \tilde{B}_{1n}(t) &= (1 - D)\tilde{G}_n(t) + \eta_2 \tilde{H}_n(t), \end{aligned} \tag{3.11}$$

and involve two further coefficients

$$\begin{aligned} \eta_1 &= 2DR_2 n^2[-\beta_{n2}(\sigma_1 - \sigma_2\xi_1) + nh_2(\tau_1 - \tau_2\xi_1)] \\ &\quad + 2R_1 n^2[\beta_{n1} - nh_1\xi_1], \\ \eta_2 &= 2DR_2 n^2[-\beta_{n2}(\sigma_3 - \sigma_2\xi_2) + nh_2(-\tau_3 - \tau_2\xi_2)] \\ &\quad - 2R_1 n^3 h_1 \xi_2. \end{aligned}$$

Finally, the linearized kinematic condition (3.3) gives two more conditions from its even and odd components, and these are

$$\begin{aligned} n(1 - D)\rho_1 \tilde{G}_n(t) - \eta_1 \tilde{G}'_n(t) &= n\rho_2 \tilde{H}_n(t), \\ n(1 - D)\rho_1 \tilde{H}_n(t) - \eta_1 \tilde{H}'_n(t) &= -n\rho_2 \tilde{G}_n(t) \end{aligned} \tag{3.12}$$

with further intermediate constants

$$\begin{aligned} \rho_1 &= -Z_{1n}(0) + Z_{2n}(0)\xi_1, \\ \rho_2 &= Z_{1n}(0)\eta_2 + Z_{2n}(0)(\xi_2\eta_1 - \xi_1\eta_2) + U_{10}(0)\eta_1. \end{aligned}$$

In these expressions, the coefficients $\tilde{A}_{1n}$ and so on have been eliminated using the previous relations (3.7)–(3.11). The two conditions in the system (3.12) are

https://doi.org/10.1017/S1446181115000085 Published online by Cambridge University Press

combined to form the following second-order ordinary differential equation with constant coefficients:

$$\eta_1^2\tilde{G}_n''(t) - 2n\rho_1(1-D)\eta_1\tilde{G}_n'(t) + [n^2\rho_1^2(1-D)^2 + n^2\rho_2^2]\tilde{G}_n(t) = 0. \tag{3.13}$$

It immediately permits solutions of the exponential form

$$\tilde{G}_n(t) = \text{constant} \times e^{\lambda t},$$

which yields the growth rate

$$\lambda = \frac{n}{\eta_1}[\rho_1(1-D) \pm i\rho_2]. \tag{3.14}$$

Thus, the real part of this expression, $n\rho_1(1-D)/\eta_1$, determines the growth in the amplitude of the disturbance and the quantity ρ_2/η_1, derived from the imaginary part, gives the speed. The differential equation (3.13) then gives the two coefficients in the linearized interface height to be

$$\tilde{G}_n(t) = \exp\left(\frac{n(1-D)\rho_1 t}{\eta_1}\right)\left[\tilde{G}_C\cos\left(\frac{n\rho_2 t}{\eta_1}\right) + \tilde{G}_S\sin\left(\frac{n\rho_2 t}{\eta_1}\right)\right],$$
$$\tilde{H}_n(t) = \exp\left(\frac{n(1-D)\rho_1 t}{\eta_1}\right)\left[\tilde{G}_C\sin\left(\frac{n\rho_2 t}{\eta_1}\right) - \tilde{G}_S\cos\left(\frac{n\rho_2 t}{\eta_1}\right)\right],$$

in which $\tilde{G}_C$ and $\tilde{G}_S$ are arbitrary constants. The other coefficients may now be obtained from these expressions, using (3.7)–(3.11).

The constants appearing in the expression (3.14) are complicated expressions that must be evaluated numerically. In all the cases we have studied, it is observed that η_1 and η_2 are positive, but ρ_1 and ρ_2 are negative. As a result, the real part of (3.14) is found to be negative when $D < 1$, so that the initial disturbance eventually decays; this might be expected on purely physical grounds in the presence of high viscosity. For $D < 1$, Pozrikidis [22] likewise argued that interfacial waves must decay over time as energy is dissipated by viscosity.

4. The nonlinear spectral method

The technique presented here for the solution of the nonlinear equations in Section 2 is an extension of the method of Forbes et al. [13], which was developed for inviscid free-surface problems. In that paper, two approaches were presented. The first assumed simply that the interface η was a single-valued function of x, and a spectral technique was developed on that basis. There was also a second approach, which those authors referred to as an "extended" method, in which the interface was represented using an arclength, so that overturning profiles could be accounted for. This second, more general, approach is followed here. Forbes et al. [13] showed that the conditions at the interface between two inviscid fluids lead to a mixed system of algebraic and differential equations; they then converted this into one governed purely by differential equations, by differentiating some of the interfacial conditions exactly with respect to

https://doi.org/10.1017/S1446181115000085 Published online by Cambridge University Press

time. This allowed the system of differential equations to be integrated forward in time, using existing routines. While that same approach has been tried here, it turns out to be simpler to use the undifferentiated boundary conditions directly, where possible. For this viscous problem, this also avoids a considerable amount of algebraic manipulation in the derivation of the algorithm. This new approach is described in this section.

Consider a single wavelength, which in dimensionless coordinates is located over an interval of width 2π along the x-axis. Let s be the arclength along the interface, which has some overall length $L_S(t)$ within a single wavelength. A time-independent arclength ξ is now defined along the interface, by means of the relation

$$\xi = \frac{2\pi s}{L_S(t)}. \tag{4.1}$$

The Pythagorean definition of arclength then leads to the condition

$$\left(\frac{\partial x}{\partial \xi}\right)^2 + \left(\frac{\partial y}{\partial \xi}\right)^2 = \frac{L_S^2(t)}{(2\pi)^2} \tag{4.2}$$

for the interface $y = \eta(x, t)$, now represented in parametric form as $(x(\xi, t), y(\xi, t))$. As yet, the surface length $L_S(t)$ is unknown. In terms of the arclength in equation (4.1), the interface is represented as

$$\begin{aligned} x(\xi, t) &= \xi + \sum_{n=1}^{N} F_n(t)\cos(n\xi) + G_n(t)\sin(n\xi), \\ y(\xi, t) &= K_0(t) + \sum_{n=1}^{N} K_n(t)\cos(n\xi) + L_n(t)\sin(n\xi). \end{aligned} \tag{4.3}$$

As with the series representations (2.12)–(2.16) in Section 2, the Fourier sums (4.3) have been truncated at some finite number N for numerical implementation, and the expressions become exact as $N \to \infty$.

The arclength condition (4.2) is now analysed into its Fourier modes. The zeroth-mode condition is obtained by substituting (4.3) directly into (4.2) and integrating over the interval $-\pi < \xi < \pi$. After a little algebra, and using the orthogonality conditions for the trigonometric functions [18, p. 482], the formula

$$L_S(t) = 2\pi\sqrt{1 + \frac{1}{2}\sum_{n=1}^{N} n^2[F_n^2(t) + G_n^2(t) + K_n^2(t) + L_n^2(t)]} \tag{4.4}$$

is obtained for the surface length of the interface along a wavelength.

As in Forbes et al. [13], the arclength condition (4.2) is differentiated with respect to time, giving

$$\left(\frac{\partial x}{\partial \xi}\right)\left(\frac{\partial^2 x}{\partial \xi \partial t}\right) + \left(\frac{\partial y}{\partial \xi}\right)\left(\frac{\partial^2 y}{\partial \xi \partial t}\right) = \frac{L_S(t)L_S'(t)}{(2\pi)^2}. \tag{4.5}$$

The higher Fourier modes for the arclength condition are obtained by decomposing equation (4.5) spectrally. The higher even modes result from multiplying (4.5) by

https://doi.org/10.1017/S1446181115000085 Published online by Cambridge University Press

$\cos(\ell\xi)$ and integrating over the interval $\xi \in [-\pi, \pi]$, and the odd modes are obtained after multiplication by basis functions $\sin(\ell\xi)$ and integrating over the same interval. Here ℓ are integers and take values $\ell = 1, 2, \ldots, N$. The second-derivative terms in (4.5) are evaluated exactly from the series (4.3) and, after some algebra, the even-mode decomposition yields the system of differential equations

$$-\sum_{n=1}^{N} n\mathcal{X}_{\ell n}^{SC} F_n'(t) + \sum_{n=1}^{N} n\mathcal{X}_{\ell n}^{CC} G_n'(t) - \sum_{n=1}^{N} n\mathcal{Y}_{\ell n}^{SC} K_n'(t) + \sum_{n=1}^{N} n\mathcal{Y}_{\ell n}^{CC} L_n'(t) = 0, \tag{4.6}$$

and the odd modes give

$$-\sum_{n=1}^{N} n\mathcal{X}_{\ell n}^{SS} F_n'(t) + \sum_{n=1}^{N} n\mathcal{X}_{\ell n}^{CS} G_n'(t) - \sum_{n=1}^{N} n\mathcal{Y}_{\ell n}^{SS} K_n'(t) + \sum_{n=1}^{N} n\mathcal{Y}_{\ell n}^{CS} L_n'(t) = 0 \tag{4.7}$$

for $\ell = 1, 2, \ldots, N$. There are eight sets of intermediate quantities in these two expressions, and they are given as follows:

$$\begin{aligned} \mathcal{X}_{\ell n}^{SC}(t) &= \int_{-\pi}^{\pi} \left(\frac{\partial x}{\partial \xi}\right) \sin(n\xi)\cos(\ell\xi)\, d\xi, \\ \mathcal{Y}_{\ell n}^{SC}(t) &= \int_{-\pi}^{\pi} \left(\frac{\partial y}{\partial \xi}\right) \sin(n\xi)\cos(\ell\xi)\, d\xi \end{aligned} \tag{4.8}$$

and so on. Each of these eight sets of quantities $\mathcal{X}_{\ell n}^{AB}$ and $\mathcal{Y}_{\ell n}^{AB}$ is coded so that $\mathcal{X}$ indicates that the first term in the integrand is $\partial x/\partial\xi$ and $\mathcal{Y}$ corresponds to $\partial y/\partial\xi$. The first superscript A is either S or C, representing the fact that the second term is either $\sin(n\xi)$ or $\cos(n\xi)$, and the second superscript B is also either S or C, similarly indicating whether the third term contains $\sin(\ell\xi)$ or $\cos(\ell\xi)$.

The chain rule of calculus is now used to re-write the two kinematic conditions (2.5) parametrically in terms of the coordinates $(x(\xi, t), y(\xi, t))$ along the interface. Further details are given by Forbes et al. [13]. The two conditions take the forms

$$\begin{aligned} v_1(\xi,t)\frac{\partial x}{\partial \xi} &= \frac{\partial y}{\partial t}\frac{\partial x}{\partial \xi} - \frac{\partial y}{\partial \xi}\frac{\partial x}{\partial t} + u_1(\xi,t)\frac{\partial y}{\partial \xi}, \\ v_2(\xi,t)\frac{\partial x}{\partial \xi} &= \frac{\partial y}{\partial t}\frac{\partial x}{\partial \xi} - \frac{\partial y}{\partial \xi}\frac{\partial x}{\partial t} + u_2(\xi,t)\frac{\partial y}{\partial \xi}. \end{aligned} \tag{4.9}$$

For the first kinematic condition in (4.9), the zeroth Fourier mode is obtained simply by integrating the equation over a period. The series (2.12) is truncated after the Nth term and differentiated using equation (2.9) to give series representations for u_1 and v_1, and these are evaluated at the interface. It follows from integration by parts that

$$\int_{-\pi}^{\pi} v_1(\xi,t)\frac{\partial x}{\partial \xi}\, d\xi = \int_{-\pi}^{\pi} u_1(\xi,t)\frac{\partial y}{\partial \xi}\, d\xi,$$

so that the zeroth-mode contribution from the first kinematic condition reduces to

$$\int_{-\pi}^{\pi} \frac{\partial y}{\partial t}\frac{\partial x}{\partial \xi}\, d\xi = \int_{-\pi}^{\pi} \frac{\partial x}{\partial t}\frac{\partial y}{\partial \xi}\, d\xi.$$

https://doi.org/10.1017/S1446181115000085 Published online by Cambridge University Press

Substituting (4.3) into this relation finally gives the result

$$K_0'(t) = \frac{d}{dt}\Big\{\frac{1}{2}\sum_{n=1}^{N} n[F_n(t)L_n(t) - G_n(t)K_n(t)]\Big\}. \tag{4.10}$$

This result is now integrated with respect to time to yield

$$\begin{aligned} K_0(t) = K_0(0) &+ \frac{1}{2}\sum_{n=1}^{N} n[F_n(t)L_n(t) - G_n(t)K_n(t)] \\ &- \frac{1}{2}\sum_{n=1}^{N} n[F_n(0)L_n(0) - G_n(0)K_n(0)]. \end{aligned} \tag{4.11}$$

The contributions for the even and odd higher-order modes from the first kinematic condition in (4.9) are obtained by multiplying by $\cos(\ell\xi)$ and $\sin(\ell\xi)$, respectively, for $\ell = 1, 2, \ldots, N$ and integrating over a period. The quantity $K_0'(t)$ is eliminated using equation (4.10), and the even component gives

$$\begin{aligned} \sum_{n=1}^{N}\Big[\frac{1}{2}n\ell\pi G_\ell(t)L_n(t) - \mathcal{Y}_{\ell n}^{CC}\Big]F_n'(t) &- \Big[\frac{1}{2}n\ell\pi G_\ell(t)K_n(t) - \mathcal{Y}_{\ell n}^{SC}\Big]G_n'(t) \\ &- \Big[\frac{1}{2}n\ell\pi G_\ell(t)G_n(t) - \mathcal{X}_{\ell n}^{CC}\Big]K_n'(t) + \Big[\frac{1}{2}n\ell\pi G_\ell(t)F_n(t) + \mathcal{X}_{\ell n}^{SC}\Big]L_n'(t) \\ &= -\ell\int_{-\pi}^{\pi}\psi_1\sin(\ell\xi)\,d\xi, \end{aligned} \tag{4.12}$$

in which the intermediate quantities are those given in equation (4.8). Similarly, the odd components in the first kinematic condition yield

$$\begin{aligned} \sum_{n=1}^{N}\Big[\frac{1}{2}n\ell\pi F_\ell(t)L_n(t) + \mathcal{Y}_{\ell n}^{CS}\Big]F_n'(t) &- \Big[\frac{1}{2}n\ell\pi F_\ell(t)K_n(t) - \mathcal{Y}_{\ell n}^{SS}\Big]G_n'(t) \\ &- \Big[\frac{1}{2}n\ell\pi F_\ell(t)G_n(t) + \mathcal{X}_{\ell n}^{CS}\Big]K_n'(t) + \Big[\frac{1}{2}n\ell\pi F_\ell(t)F_n(t) - \mathcal{X}_{\ell n}^{SS}\Big]L_n'(t) \\ &= -\ell\int_{-\pi}^{\pi}\psi_1\cos(\ell\xi)\,d\xi. \end{aligned} \tag{4.13}$$

Equations (4.6), (4.7), (4.12) and (4.13) constitute a system of $4N$ ordinary differential equations in time, for the $4N$ quantities $F_n(t)$, $G_n(t)$, $K_n(t)$ and $L_n(t)$. Assuming that all the variables are known at time level t_k, we use Euler's method to integrate this system of differential equations to the next time level $t_{k+1} = t_k + \Delta t$. From the values of these four sets of coefficients, the shape of the interface $(x(\xi, t), y(\xi, t))$ is now constructed at the new time level t_{k+1} using equations (4.11) and (4.3).

The coefficients defining the two streamfunctions in the representations (2.12) and (2.13) are now determined at the new time level t_{k+1}. With the shape of the interface now known at this time level, the remaining boundary conditions (2.6)–(2.8) are linear

https://doi.org/10.1017/S1446181115000085 Published online by Cambridge University Press

in the velocity components and pressure at the interface, and so the coefficients can be obtained simply by solving a linear matrix system of equations at the new time step. These equations are obtained by Fourier decomposition of the remaining four boundary conditions.

It is straightforward to show that the second kinematic condition in the system (4.9) is redundant, and so can be ignored in favour of the two no-slip boundary conditions (2.6). The first of these is written as $u_1 - u_2 = 0$ on the interface, and the representations (2.12), (2.13) and (4.3) are substituted into this equation. The even Fourier modes are then obtained by multiplying by basis functions $\cos(\ell\xi)$ for $\ell = 1, 2, \ldots, N$ and integrating over the interval $[-\pi, \pi]$. This gives a system of algebraic equations in the form

$$\begin{aligned}\sum_{n=1}^{N}&[C_{\ell n}^{U1A}A_{1n}(t) + C_{\ell n}^{U1B}B_{1n}(t) + C_{\ell n}^{U1C}C_{1n}(t) + C_{\ell n}^{U1D}D_{1n}(t)]\\ &- [C_{\ell n}^{U2A}A_{2n}(t) + C_{\ell n}^{U2B}B_{2n}(t) + C_{\ell n}^{U2C}C_{2n}(t) + C_{\ell n}^{U2D}D_{2n}(t)]\\ &= \frac{\pi(F_2 - F_1)(R_1 - DR_2)}{(h_2R_1 + h_1DR_2)}K_\ell(t)\end{aligned} \tag{4.14}$$

at the new time level $t = t_{k+1}$. Similarly, the odd Fourier modes are obtained after multiplication by the basis functions $\sin(\ell\xi)$ and integration, and give rise to the system

$$\begin{aligned}\sum_{n=1}^{N}&[S_{\ell n}^{U1A}A_{1n}(t) + S_{\ell n}^{U1B}B_{1n}(t) + S_{\ell n}^{U1C}C_{1n}(t) + S_{\ell n}^{U1D}D_{1n}(t)]\\ &- [S_{\ell n}^{U2A}A_{2n}(t) + S_{\ell n}^{U2B}B_{2n}(t) + S_{\ell n}^{U2C}C_{2n}(t) + S_{\ell n}^{U2D}D_{2n}(t)]\\ &= \frac{\pi(F_2 - F_1)(R_1 - DR_2)}{(h_2R_1 + h_1DR_2)}L_\ell(t).\end{aligned} \tag{4.15}$$

In these two sets of expressions, intermediate quantities

$$\begin{aligned}C_{\ell n}^{U1A}(t) &= \int_{-\pi}^{\pi} Z'_{1n}(y)\cos(nx)\cos(\ell\xi)\,d\xi,\\ C_{\ell n}^{U1B}(t) &= \int_{-\pi}^{\pi} Z'_{1n}(y)\sin(nx)\cos(\ell\xi)\,d\xi,\\ C_{\ell n}^{U1C}(t) &= \int_{-\pi}^{\pi} Z'_{2n}(y)\cos(nx)\cos(\ell\xi)\,d\xi,\\ C_{\ell n}^{U1D}(t) &= \int_{-\pi}^{\pi} Z'_{2n}(y)\sin(nx)\cos(\ell\xi)\,d\xi\end{aligned} \tag{4.16}$$

have been defined for convenience, and the quantities Z_{1n} and so on are defined in (2.14). The further intermediate terms $C_{\ell n}^{U2A}$ and $C_{\ell n}^{U2B}$ are identical to $C_{\ell n}^{U1A}$ and $C_{\ell n}^{U1B}$, respectively, in equation (4.16) except that Z'_{1n} must be replaced by Z'_{3n}. Similarly, $C_{\ell n}^{U2C}$ and $C_{\ell n}^{U2D}$ are obtained from $C_{\ell n}^{U1C}$ and $C_{\ell n}^{U1D}$ by replacing Z'_{2n} with Z'_{4n}. The quantity $S_{\ell n}^{U1A}$ is derived from $C_{\ell n}^{U1A}$ by replacing $\cos(\ell\xi)$ with $\sin(\ell\xi)$ in the integrand, and so on for the other similar terms.

https://doi.org/10.1017/S1446181115000085 Published online by Cambridge University Press

The second of the no-slip conditions (2.6) is written as $v_1 - v_2 = 0$ and also subjected to Fourier analysis. The even modes give rise to a system of algebraic equations

$$\sum_{n=1}^{N}[C_{\ell n}^{V1A}A_{1n}(t) - C_{\ell n}^{V1B}B_{1n}(t) + C_{\ell n}^{V1C}C_{1n}(t) - C_{\ell n}^{V1D}D_{1n}(t) - C_{\ell n}^{V2A}A_{2n}(t) + C_{\ell n}^{V2B}B_{2n}(t) - C_{\ell n}^{V2C}C_{2n}(t) + C_{\ell n}^{V2D}D_{2n}(t)] = 0, \tag{4.17}$$

and the odd modes likewise lead to a further system of equations in the form

$$\sum_{n=1}^{N}[S_{\ell n}^{V1A}A_{1n}(t) - S_{\ell n}^{V1B}B_{1n}(t) + S_{\ell n}^{V1C}C_{1n}(t) - S_{\ell n}^{V1D}D_{1n}(t) - S_{\ell n}^{V2A}A_{2n}(t) + S_{\ell n}^{V2B}B_{2n}(t) - S_{\ell n}^{V2C}C_{2n}(t) + S_{\ell n}^{V2D}D_{2n}(t)] = 0, \quad \ell = 1, 2, \ldots, N. \tag{4.18}$$

Again, a number of intermediate quantities have been defined in these expressions, as integrals involving the known interface shape $(x(\xi, t), y(\xi, t))$ at the new time level t_{k+1}. The first of these are

$$\begin{aligned} C_{\ell n}^{V1A}(t) &= n\int_{-\pi}^{\pi} Z_{1n}(y)\sin(nx)\cos(\ell\xi)\,d\xi, \\ C_{\ell n}^{V1B}(t) &= n\int_{-\pi}^{\pi} Z_{1n}(y)\cos(nx)\cos(\ell\xi)\,d\xi, \\ C_{\ell n}^{V1C}(t) &= n\int_{-\pi}^{\pi} Z_{2n}(y)\sin(nx)\cos(\ell\xi)\,d\xi, \\ C_{\ell n}^{V1D}(t) &= n\int_{-\pi}^{\pi} Z_{2n}(y)\cos(nx)\cos(\ell\xi)\,d\xi. \end{aligned} \tag{4.19}$$

As previously, $C_{\ell n}^{V2A}$ and $C_{\ell n}^{V2B}$ are obtained from $C_{\ell n}^{V1A}$ and $C_{\ell n}^{V1B}$, respectively, by replacing Z_{1n} with Z_{3n}, and the quantities $C_{\ell n}^{V2C}$ and $C_{\ell n}^{V2D}$ are derived from $C_{\ell n}^{V1C}$ and $C_{\ell n}^{V1D}$, respectively, by substituting Z_{4n} in place of Z_{2n}. Finally, the odd terms $S_{\ell n}^{V1A}$ and so on are the same as the even terms $C_{\ell n}^{V1A}$ and so on, except that $\cos(\ell\xi)$ must be replaced by $\sin(\ell\xi)$ in the integrands of these expressions.

In the arclength variable ξ, the tangential dynamic condition (2.7) at the interface takes the form

$$DR_2[-2x_\xi y_\xi u_{2X} + \tfrac{1}{2}(x_\xi^2 - y_\xi^2)(u_{2Y} + v_{2X})] = R_1[-2x_\xi y_\xi u_{1X} + \tfrac{1}{2}(x_\xi^2 - y_\xi^2)(u_{1Y} + v_{1X})],$$

in which the functions u_{1X} and u_{1Y} represent the derivatives of the velocity component $u_1(x, y, t)$ with respect to x and y, respectively, holding the other variables constant, and then evaluated at the interface $(x(\xi, t), y(\xi, t))$, and similarly for the other velocity components. The velocity components and their derivatives in this relation are obtained from the series representations (2.12) and (2.13) by differentiation, following

https://doi.org/10.1017/S1446181115000085 Published online by Cambridge University Press

equations (2.9). The resulting expression is again subject to Fourier analysis, in both its even and odd components. After some algebra, the even components of the tangential dynamic condition give a system of equations of the form

$$R_1 \sum_{n=1}^{N} [T_{\ell n}^{1AC} A_{1n}(t) + T_{\ell n}^{1BC} B_{1n}(t) + T_{\ell n}^{1CC} C_{1n}(t) + T_{\ell n}^{1DC} D_{1n}(t)] = DR_2 \sum_{n=1}^{N} [T_{\ell n}^{2AC} A_{2n}(t) + T_{\ell n}^{2BC} B_{2n}(t) + T_{\ell n}^{2CC} C_{2n}(t) + T_{\ell n}^{2DC} D_{2n}(t)], \quad (4.20)$$

and the odd Fourier modes give the corresponding system of equations

$$R_1 \sum_{n=1}^{N} [T_{\ell n}^{1AS} A_{1n}(t) + T_{\ell n}^{1BS} B_{1n}(t) + T_{\ell n}^{1CS} C_{1n}(t) + T_{\ell n}^{1DS} D_{1n}(t)] = DR_2 \sum_{n=1}^{N} [T_{\ell n}^{2AS} A_{2n}(t) + T_{\ell n}^{2BS} B_{2n}(t) + T_{\ell n}^{2CS} C_{2n}(t) + T_{\ell n}^{2DS} D_{2n}(t)]. \quad (4.21)$$

There are again further intermediate quantities in these expressions, and the first two of these are

$$\begin{aligned} T_{\ell n}^{1AC}(t) &= \int_{-\pi}^{\pi} \Big[2nx_\xi y_\xi Z_{1n}'(y) \sin(nx) + \frac{1}{2}(x_\xi^2 - y_\xi^2)\{Z_{1n}''(y) \\ &\qquad + n^2 Z_{1n}(y)\} \cos(nx) \Big] \cos(\ell\xi)\, d\xi, \\ T_{\ell n}^{1BC}(t) &= \int_{-\pi}^{\pi} \Big[-2nx_\xi y_\xi Z_{1n}'(y) \cos(nx) + \frac{1}{2}(x_\xi^2 - y_\xi^2)\{Z_{1n}''(y) \\ &\qquad + n^2 Z_{1n}(y)\} \sin(nx) \Big] \cos(\ell\xi)\, d\xi. \end{aligned} \quad (4.22)$$

The functions $T_{\ell n}^{1CC}$ and $T_{\ell n}^{1DC}$ are next obtained from these two functions (4.22) by replacing the function Z_{1n} with Z_{2n} everywhere. Similarly, $T_{\ell n}^{2AC}$ and $T_{\ell n}^{2BC}$ are obtained from (4.22) by replacing Z_{1n} with Z_{3n}, and $T_{\ell n}^{2CC}$ and $T_{\ell n}^{2DC}$ result by substituting the function Z_{4n}. The intermediate quantities $T_{\ell n}^{1AS}$ and so on, in which the symbol S appears in the superscript, are derived from these by replacing the even basis functions $\cos(\ell\xi)$ with the corresponding odd functions $\sin(\ell\xi)$.

Finally, the normal dynamic condition (2.8) at the interface may be written as

$$\begin{aligned} p_2 \frac{L_S^2(t)}{(2\pi)^2} + 2DR_2[(x_\xi^2 - y_\xi^2)u_{2X} + x_\xi y_\xi(u_{2Y} + v_{2X})] \\ = p_1 \frac{L_S^2(t)}{(2\pi)^2} + 2R_1[(x_\xi^2 - y_\xi^2)u_{1X} + x_\xi y_\xi(u_{1Y} + v_{1X})] \\ + \frac{2\pi\sigma}{L_S(t)}(x_\xi y_{\xi\xi} - y_\xi x_{\xi\xi}) \end{aligned}$$

in terms of the scaled arclength variable ξ. Here, σ is the surface-tension coefficient and $L_S(t)$ is the length of the interface over one period, for which an expression is

https://doi.org/10.1017/S1446181115000085 Published online by Cambridge University Press

derived in equation (4.4). This relation is now subject to Fourier decomposition, as before, in both its even and odd Fourier modes. The even components yield a relation of the form

$$\begin{aligned}
&2R_1 \sum_{n=1}^{N} [N_{\ell n}^{1AC} A_{1n}(t) + N_{\ell n}^{1BC} B_{1n}(t) + N_{\ell n}^{1CC} C_{1n}(t) + N_{\ell n}^{1DC} D_{1n}(t)] \\
&\quad - 2DR_2 \sum_{n=1}^{N} [N_{\ell n}^{2AC} A_{2n}(t) + N_{\ell n}^{2BC} B_{2n}(t) + N_{\ell n}^{2CC} C_{2n}(t) + N_{\ell n}^{2DC} D_{2n}(t)] \\
&\quad = -(D-1)\frac{L_S^2(t)}{(2\pi)^2}\pi K_\ell(t) - \frac{2\pi\sigma}{L_S(t)} \int_{-\pi}^{\pi} (x_\xi y_{\xi\xi\xi} - y_\xi x_{\xi\xi\xi}) \cos(\ell\xi)\, d\xi,
\end{aligned} \tag{4.23}$$

while the odd components give

$$\begin{aligned}
&2R_1 \sum_{n=1}^{N} [N_{\ell n}^{1AS} A_{1n}(t) + N_{\ell n}^{1BS} B_{1n}(t) + N_{\ell n}^{1CS} C_{1n}(t) + N_{\ell n}^{1DS} D_{1n}(t)] \\
&\quad - 2DR_2 \sum_{n=1}^{N} [N_{\ell n}^{2AS} A_{2n}(t) + N_{\ell n}^{2BS} B_{2n}(t) + N_{\ell n}^{2CS} C_{2n}(t) + N_{\ell n}^{2DS} D_{2n}(t)] \\
&\quad = -(D-1)\frac{L_S^2(t)}{(2\pi)^2}\pi L_\ell(t) - \frac{2\pi\sigma}{L_S(t)} \int_{-\pi}^{\pi} (x_\xi y_{\xi\xi\xi} - y_\xi x_{\xi\xi\xi}) \sin(\ell\xi)\, d\xi.
\end{aligned} \tag{4.24}$$

The two equations (4.23) and (4.24) again involve a number of intermediate products, defined as integrals, similar to (4.22) used for the tangential stress condition. The first two are

$$\begin{aligned}
N_{\ell n}^{1AC}(t) &= \int_{-\pi}^{\pi} \Big[-n(x_\xi^2 - y_\xi^2) Z_{1n}'(y) \sin(nx) - n^2 \frac{L_S^2(t)}{(2\pi)^2} W_{1n}(y) \sin(nx) \\
&\qquad + x_\xi y_\xi (Z_{1n}''(y) + n^2 Z_{1n}(y)) \cos(nx) \Big] \cos(\ell\xi)\, d\xi, \\
N_{\ell n}^{1BC}(t) &= \int_{-\pi}^{\pi} \Big[n(x_\xi^2 - y_\xi^2) Z_{1n}'(y) \cos(nx) + n^2 \frac{L_S^2(t)}{(2\pi)^2} W_{1n}(y) \cos(nx) \\
&\qquad + x_\xi y_\xi (Z_{1n}''(y) + n^2 Z_{1n}(y)) \sin(nx) \Big] \cos(\ell\xi)\, d\xi.
\end{aligned} \tag{4.25}$$

The next two intermediate functions $N_{\ell n}^{1CC}$ and $N_{\ell n}^{1DC}$ are obtained from the quantities in (4.25) by replacing all occurrences of the function Z_{1n} with Z_{2n} and W_{1n} with $-W_{2n}$. Then $N_{\ell n}^{2AC}$ and $N_{\ell n}^{2BC}$ are created from (4.25) by replacing Z_{1n} and W_{1n} with Z_{3n} and W_{3n}, respectively, while $N_{\ell n}^{2CC}$ and $N_{\ell n}^{2DC}$ are generated from (4.25) by replacing Z_{1n} and W_{1n} with Z_{4n} and $-W_{4n}$, respectively. Finally, quantities with an S superscript, such as $N_{\ell n}^{1AS}$, are obtained from the corresponding term with a C superscript, such as $N_{\ell n}^{1AC}$, by replacing $\cos(\ell\xi)$ in the integrand with $\sin(\ell\xi)$.

The eight sets of coefficients A_{1n}, B_{1n}, C_{1n}, D_{1n}, A_{2n}, B_{2n}, C_{2n} and D_{2n} are now calculated at the new time level t_{k+1} by solving the system of $8N$ linear algebraic equations (4.14), (4.15), (4.17), (4.18), (4.20), (4.21), (4.23) and (4.24). The coefficients of this matrix equation involve the intermediate quantities (4.16), (4.19),

https://doi.org/10.1017/S1446181115000085 Published online by Cambridge University Press

(4.22) and (4.25), and these integral terms were evaluated using Gaussian quadrature over an interfacial grid of 401 points, using the routine written by von Winckel [28]. (The previous intermediate functions in equations (4.8) were evaluated using the same quadrature routine.)

Since the integration of the arclength equation and first kinematic equation was done simply using Euler's method, a large number of time steps was needed in order to maintain accuracy. This was accomplished in the algorithm using two nested loops; the inner loop typically took 1000 time steps and was embedded in an outer loop of about 30 steps. This enabled the output to be generated only at the 30 times of interest. In addition, we found that the interface could develop small numerical instabilities, which were visible as oscillations on the wave profile, with wavenumber equal to that of the highest Fourier mode, N, included in the computation. This is a well-known numerical difficulty in the computation of the Kelvin–Helmholtz instability, and has been discussed widely in the literature. To overcome this difficulty, Krasny [17] introduced a type of *vortex blob* method, in which the sharp interface was effectively smudged over a region of finite width. This technique has received considerable attention, and Baker and Pham [2] considered several approaches of this type, and showed that they did, in fact, somehow alter the evolution of the unstable flow. Chen and Forbes [6] used a five-point difference formula to smooth the interface in their calculation, and Forbes and Cosgrove [14] penalized the higher Fourier modes using apodization in their investigation of a Kelvin–Helmholtz type instability in cylindrical geometry. In the present algorithm, we have applied a sensitive smoothing approach to the interface, and only in about 30 steps of the outer time loop in our method. The idea is based on Lanczos smoothing, as discussed in the text by Hamming [15, p. 535]. The Fourier-series representations for the functions $x(\xi, t)$ and $y(\xi, t)$ in equations (4.3) at some spatial point ξ_j are replaced with their spatial *average* over some narrow interval, $\xi_j - \sigma_L < \xi < \xi_j + \sigma_L$, about the point of interest. A straightforward calculation then shows that this is equivalent to replacing the coefficients F_n, G_n K_n and L_n in equations (4.3) by their present values multiplied by $\sin(n\sigma_L)/(n\sigma_L)$, $n = 1, 2, \ldots, N$. This is particularly easy to implement and, with $\sigma_L \approx 0.05$, can remove many of the spurious instabilities in the wave profile. It must, however, be admitted candidly that this smoothing process does change the results to some extent, a feature which it shares in common with other techniques such as the *vortex blob* method [2]. To monitor errors, therefore, the residuals of the arclength equation (4.2), the two no-slip conditions (2.6) and the tangential and normal dynamic conditions at the interface are plotted, and their deviation from zero is noted. This helps to guide the choice of the Lanczos parameter σ_L.

Some comments on the initial conditions are appropriate. In order to be consistent with the linearized solution in Section 3 and results reported in the literature, it is desirable to start the solution with the pure cosine profile

$$\eta(x, 0) = \epsilon \cos(n_M x), \tag{4.26}$$

in which the integer n_M gives the desired mode of the perturbation to the interface, and ϵ is its amplitude. From the arclength condition (4.2) and the desired profile (4.26), it

https://doi.org/10.1017/S1446181115000085 Published online by Cambridge University Press

follows that the total initial interface length is

$$L_S(0) = \int_{-\pi}^{\pi} \sqrt{1 + \epsilon^2 n_M^2 \sin^2(n_M \xi)}\, d\xi.$$

This is, in fact, a complete elliptic integral of the second kind (see Abramowitz and Stegun [1, p. 590]), but here it is evaluated using von Winckel's Gaussian quadrature routine [28]. A simple Euler method approach is used to solve the differential equation

$$\frac{dx}{d\xi} = \frac{L_S(0)}{2\pi \sqrt{1 + \epsilon^2 n_M^2 \sin^2(n_M x)}} \tag{4.27}$$

to get $x(\xi, 0)$. The relation (4.27) coupled with (4.26) then gives the desired initial cosine profile for the wave; this is Fourier analysed to provide starting values for the coefficients $F_n(0)$, $G_n(0)$, $K_n(0)$ and $L_n(0)$. Initial values for the coefficients $A_{1n}(0)$, and so on, are then constructed from these using the relations in Section 3 obtained from the linearized solution.

The algorithm is found to give good accuracy with about $N = 31$ Fourier coefficients, and using 401 mesh points in each period, over the interval $\xi \in [-\pi, \pi]$. As Euler's method has been used to advance the differential equations (4.6), (4.7), (4.12) and (4.13) from one numerical time level to the next, we have taken a large overall number of steps to ensure accuracy. Typically about 30 000 time steps are used, with two embedded loops so as to enable smoothing, analysis of the results and error checking, as outlined above. In such cases, the routine takes several hours run time on a moderate-sized personal computer, using *MATLAB*, and so is not overly demanding in its use of resources.

5. Presentation of results

5.1. Results with equal densities $D = 1$ To begin this presentation of results, the new spectral method described in Section 4 has been run for the case of equal fluid densities, $D = 1$. This permits some comparison with the results of Pozrikidis [22], who refers to this simple case as *shear-driven flow*. The fluid viscosities (inverse Reynolds numbers) are set to be equal, $R_1 = R_2 = 1$, the fluid depths in each layer are also equal, $h_1 = h_2 = 1$, and the speeds are anti-symmetric, with $F_1 = 1$, $F_2 = -1$. The linearized solution in Section 3 is then neutrally stable, so that equation (3.14) gives a zero exponent. A small value of surface tension, $\sigma = 0.001$, was chosen with the intention of suppressing small *wiggles* in the solution profile, although, in fact, the result is not noticeably different if surface tension is set to zero in this case. However, the Lanczos smoothing parameter was chosen to be $\sigma_L = 0.07$, since trial and error indicated that this was the largest value that could be chosen so that the results would not be affected, but that numerical wiggles in the wave profile would largely be eliminated.

The wave profile for this case is shown in Figure 2(a) and the curvature in Figure 2(b), for the three different times $t = 0.1$, 1 and 2.3. As time progresses,

https://doi.org/10.1017/S1446181115000085 Published online by Cambridge University Press

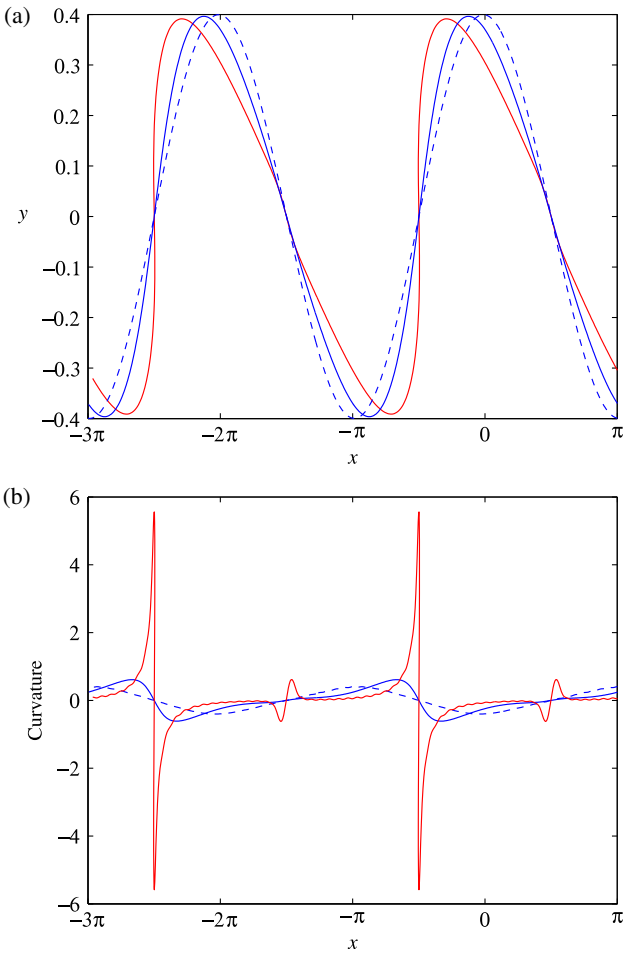

FIGURE 2. Nonlinear (a) interface shapes and (b) curvatures obtained for equal densities $D = 1$, with speeds $F_1 = 1$, $F_2 = -1$, viscosities $R_1 = R_2 = 1$ and fluid depths $h_1 = h_2 = 1$. The surface-tension parameter is $\sigma = 0.001$ and the Lanczos smoothing parameter is $\sigma_L = 0.07$. The initial amplitude was $\epsilon = 0.4$. Results are shown for the three times $t = 0.1$ (dashed line), $t = 1$ (blue online) and $t = 2.3$ (red online). (Colour available online.)

the wave profiles in Figure 2(a) lean progressively to the left, and their amplitude decreases very slightly due primarily to the effects of the fluid viscosity. Thus, the largest profile sketched with a dashed line corresponds to $t = 0.1$, the middle profile represents $t = 1$ and the most distorted one is taken from a solution with $t = 2.3$. At later times, the solution algorithm of Section 4 gave rise to an $8N \times 8N$ matrix for the Fourier coefficients that was too ill-conditioned to invert, and the method consequently failed. This will be discussed in more detail in this paper. The solution was started from a pure cosine shape, as in equation (4.26), with amplitude $\epsilon = 0.4$, and the results

https://doi.org/10.1017/S1446181115000085 Published online by Cambridge University Press

in Figure 2 were generated with $N = 31$ Fourier coefficients and 401 spatial points per wavelength, since this was found to be sufficient to guarantee solutions that are independent of these numerical details. For ease of viewing, two wavelengths have been shown in Figure 2. As the wave evolves in time, it leans to the left and develops a very narrow overhanging portion near the neutral height $y = 0$. A second region of high curvature also forms on the *back* of the wave.

One of the advantages of the new spectral algorithm outlined in Section 4 is that quantities involving derivatives of the wave profile can be evaluated with high accuracy, since exact differentiation of the series (4.3) is able to be carried out easily. From the work of Moore [20] in the purely inviscid Kelvin–Helmholtz problem, it is to be expected that the curvature is of primary interest, and it may be calculated from the well-known formula

$$\text{Curvature} = \frac{\eta_{xx}}{[1 + \eta_x^2]^{3/2}} \tag{5.1}$$

given in Kreyszig [18, p. 400]. When this is represented in terms of the arclength parameter ξ in equation (4.1), it becomes

$$\text{Curvature} = \frac{x_\xi y_{\xi\xi} - y_\xi x_{\xi\xi}}{[x_\xi^2 + y_\xi^2]^{3/2}}, \tag{5.2}$$

and this may be evaluated to high accuracy from the series representations in the spectral method.

The interfacial curvature for this case is shown in Figure 2(b) for the same three times as presented in Figure 2(a). At the earliest time $t = 0.1$, the curvature is drawn with a dashed line and it is very accurately predicted by simply the second derivative of the initial wave profile (4.26) with respect to x, as would be expected from a linearized solution. However, by the intermediate time $t = 1$, the curvature has developed a distinctly nonlinear profile, with a steep gradient at about $x = -\pi/2$. At the last time shown, $t = 2.3$, the curvature has developed a very large double peak at this value of x and, in fact, the algorithm fails to yield solutions for larger times. A smaller double peak in curvature appears to be forming at about $x = \pi/2$, on the *back* of the wave now sloping to the left at this value of time.

The behaviour of the curvature in Figure 2(b) is very reminiscent indeed of its behaviour in the purely inviscid case, as shown by Chen and Forbes [6], for example. In spite of the large viscosities assumed in the Stokes equations (2.3) and (2.4), it is nevertheless the case that the curvature grows rapidly at what was originally the inflection point on the left-hand side of the wave. As time increases, that portion of the wave steepens to the extent that it overhangs slightly, at which time the numerical results strongly suggest that a curvature singularity is formed, analogously to the Moore singularity [20] formed at finite time for the purely inviscid Kelvin–Helmholtz instability.

In order to gain an appreciation of how the wave evolves in time, a perspective-type diagram is given in Figure 3, in which the time axis points away from the viewer. Initially, the wave is a pure cosine of amplitude $\epsilon = 0.4$, and the other parameters

https://doi.org/10.1017/S1446181115000085 Published online by Cambridge University Press

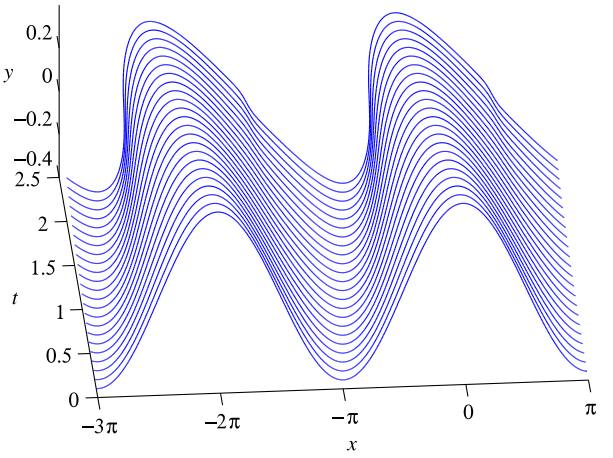

FIGURE 3. Nonlinear interface shapes for 23 times $t = 0.1, 0.2, \ldots, 2.3$, for equal densities $D = 1$, speeds $F_1 = 1$, $F_2 = -1$, viscosities $R_1 = R_2 = 1$ and fluid depths $h_1 = h_2 = 1$. The surface-tension parameter is $\sigma = 0.001$ and the Lanczos smoothing parameter is $\sigma_L = 0.07$. The initial amplitude was $\epsilon = 0.4$.

are the same as in Figure 2. Again, the solution is shown over two wave periods $-3\pi < x < \pi$ for ease of viewing. As time progresses, the interface can clearly be seen to tip towards the left, eventually developing a narrow overhanging region on the left-hand side. The development of the small ridge on the right-hand side of the wave, at about the neutral height $y = 0$, can also be seen, and this gives rise to the smaller secondary curvature spike in Figure 2(b).

It is well known that the full Kelvin–Helmholtz instability can give rise to pronounced overhanging portions at the interface, leading to the development of *cat's eyes* spirals. In the Stokes approximation (2.1), Pozrikidis [22] also obtained long finger-like intrusions of each fluid into the other. In the results presented in Figures 2 and 3, however, such intrusions were not observed, due to the formation of apparent curvature singularities midway down the overturning portion of the interface. Nevertheless, strongly overturning interfaces *may* be generated, by increasing the amount of smoothing applied to the interface. This is illustrated in Figure 4, which has been obtained with precisely the same parameters as for Figure 2, except that the Lanczos smoothing parameter has now been increased to $\sigma_L = 0.2$. Recall from Section 4 that Lanczos smoothing is only applied very sparingly in this algorithm, in an outer loop rather than at every time step. However, even such a minor increase in the level of interface smoothing can have major effects upon the solution.

From Figure 4(a), it may be seen that simply increasing the Lanczos parameter to $\sigma_L = 0.2$ now permits the solution to be continued to much later times, well beyond that at which the apparent curvature singularity had been formed in Figure 2. Two interfaces are presented in Figure 4(a); the larger amplitude profile corresponds to time $t = 1$, and is the same as the profile in Figure 2(a) obtained at the same time,

https://doi.org/10.1017/S1446181115000085 Published online by Cambridge University Press

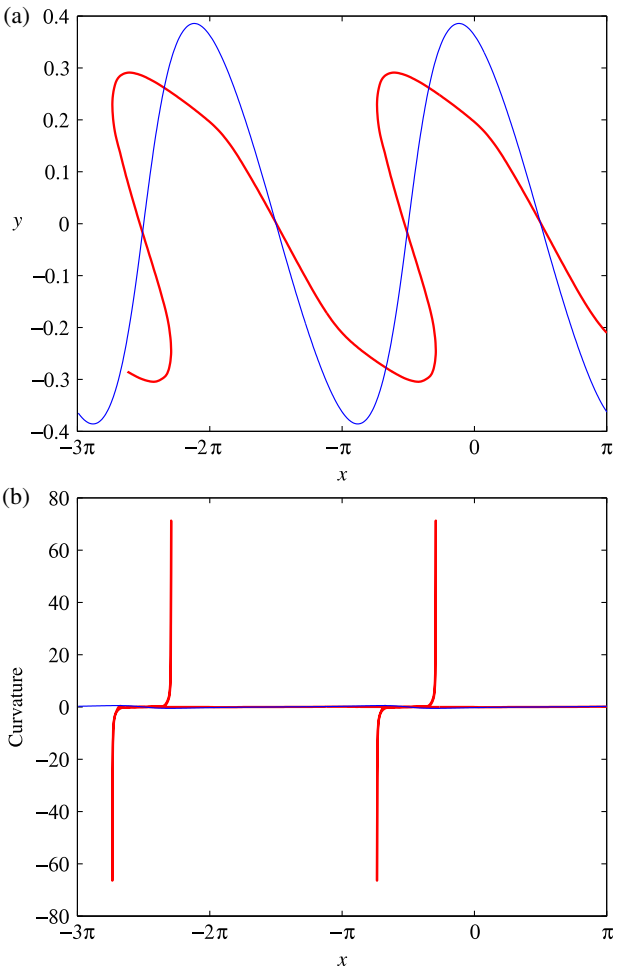

FIGURE 4. Nonlinear (a) interface shapes and (b) curvatures obtained for equal densities $D = 1$, with speeds $F_1 = 1$, $F_2 = -1$, viscosities $R_1 = R_2 = 1$ and fluid depths $h_1 = h_2 = 1$. The surface-tension parameter is $\sigma = 0$ and the Lanczos smoothing parameter is increased to $\sigma_L = 0.2$. The initial amplitude was $\epsilon = 0.4$. Results are shown at the two times $t = 1$ (blue online) and $t = 6.8$ (thick; red online). (Colour available online.)

but the strongly distorted profile, sketched with a thicker line, was produced at time $t = 6.8$. It possesses a well-developed overhanging portion, and also contains sections where the slope of the interface changes abruptly.

The curvature corresponding to this interface at the increased value $\sigma_L = 0.2$ is displayed in Figure 4(b). The result for time $t = 1$ is included in the diagram, but is almost completely overshadowed by that at the later time $t = 6.8$, sketched with a thicker line. It shows extremely large spikes in curvature, located roughly at each of the two ends of the overturned portion of the wave, where there is a sharp corner in

https://doi.org/10.1017/S1446181115000085 Published online by Cambridge University Press

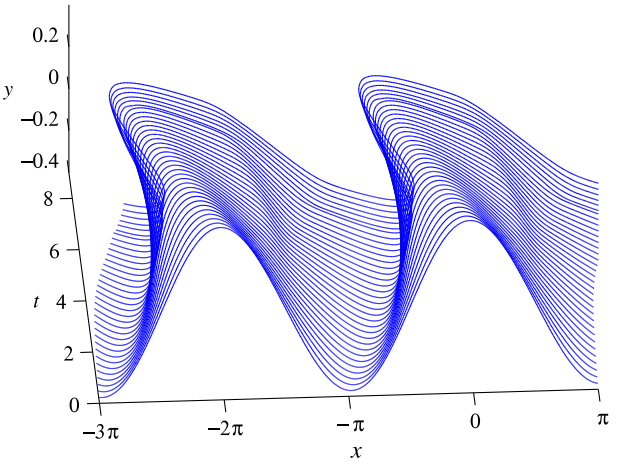

FIGURE 5. Nonlinear interface shapes for 34 times $t = 0.2, 0.4, \ldots, 6.8$, for equal densities $D = 1$, speeds $F_1 = 1$, $F_2 = -1$, viscosities $R_1 = R_2 = 1$ and fluid depths $h_1 = h_2 = 1$. The surface-tension parameter is $\sigma = 0$ and the Lanczos smoothing parameter is increased to $\sigma_L = 0.2$. The initial amplitude was $\epsilon = 0.4$.

the profile. Figure 4(b) demonstrates the accuracy that is available from this semi-numerical spectral technique.

A perspective-type diagram of the evolution of the interface, with this increased Lanczos parameter $\sigma_L = 0.2$, is presented in Figure 5. Solutions are shown at 34 different times, from $t = 0.2$ until $t = 6.8$, and they illustrate how the initial cosine profile leans to the left and then forms the strongly overhanging portions with interpenetrating fingers of fluid. The development of a small secondary ridge on the back of the wave is also visible in this diagram.

The solution profiles and curvature shown in Figures 4 and 5 are broadly similar to those obtained at other parameter values. As an example, Figure 6 presents a solution at the slower fluid speeds $F_1 = 0.1$ and $F_2 = -0.1$ and zero surface tension, while the other parameters are maintained at their previous values. The result is quite similar to that shown in Figure 4(a), except that the evolution of the interface occurs over a much longer time. Thus, the profile sketched with a dashed line in Figure 6 shows the interface at time $t = 2$, and it is almost indistinguishable from the initial cosine shape (4.26) at $t = 0$ (with $n_M = 1$). The middle curve drawn with a solid line shows the interface at time $t = 30$, when it has clearly distorted to the left. In this diagram, the Lanczos smoothing parameter has again been set to $\sigma_L = 0.2$, and this permits the interface at the last time $t = 76$ to distort heavily to the left, as shown with the thick solid line in the diagram. It has again developed pronounced overhanging portions in the profile, with regions of very high curvature at each end of the overhanging portion.

5.2. Asymptotic theory for equal densities $D = 1$ The development of apparent curvature singularities, as illustrated in Figure 4, has not been reported previously and is a surprising outcome. Accordingly, it is important to understand the origins

https://doi.org/10.1017/S1446181115000085 Published online by Cambridge University Press

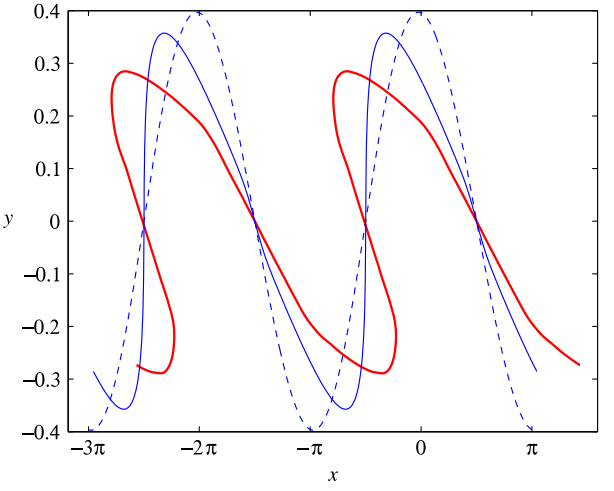

FIGURE 6. Nonlinear interface shapes obtained for equal densities $D = 1$, with speeds $F_1 = 0.1$, $F_2 = -0.1$, viscosities $R_1 = R_2 = 1$ and fluid depths $h_1 = h_2 = 1$. The surface-tension parameter is $\sigma = 0$ and the Lanczos smoothing parameter is $\sigma_L = 0.2$. The initial amplitude was $\epsilon = 0.4$. Results are shown at the three times $t = 2$ (dashed line), $t = 30$ (solid; blue online) and $t = 76$ (thick; red online). (Colour available online.)

of such behaviour. It is now shown here that curvature singularity is an inevitable consequence of the shear-driven nature of these flows, and this can be demonstrated for the degenerate case $D = 1$ in closed form.

Set $D = 1$ and the viscosities equal, $R_1 = R_2$, and, to simplify the algebra, also take the depths and speeds to be equal, so that $h_1 = h_2$ and $F_1 = -F_2$. Then the streamfunctions (2.11) both reduce to

$$\psi_1(y) = \psi_2(y) = -\frac{F_1}{2h_1}(y^2 + h_1^2).$$

This is a pure Couette flow, and it follows from equation (2.9) that the velocity is purely horizontal with components $u = -F_1 y/h_1$ and $v = 0$, as expected.

Now consider the initial wave profile (4.26) represented parametrically in the form

$$(x(0), y(0)) = (X, \epsilon \cos(n_M X)). \tag{5.3}$$

If the flow is regarded as purely Couette with the velocity remaining horizontal, then it follows that the wave profile (5.3) evolves in time to become

$$(x(t), y(t)) = \left(X - \epsilon t \frac{F_1}{h_1} \cos(n_M X), \epsilon \cos(n_M X)\right) \tag{5.4}$$

in terms of the spatial parameter X. The curvature (5.1) is again expressed parametrically, and takes the form

$$\text{Curvature} = \frac{x_X y_{XX} - y_X x_{XX}}{[x_X^2 + y_X^2]^{3/2}}, \tag{5.5}$$

https://doi.org/10.1017/S1446181115000085 Published online by Cambridge University Press

analogously to equation (5.2). We now take the parametrized waveform (5.4) and substitute into the formula (5.5) for the curvature. This yields the result

$$\text{Curvature} = -\frac{\epsilon n_M \cos(n_M X)}{[(1 + p_M(X)F_1 t/h_1)^2 + p_M^2(X)]^{3/2}}, \tag{5.6}$$

in which it is convenient to define the function

$$p_M(X) = \epsilon n_M \sin(n_M X).$$

This formula (5.6) has some fascinating consequences. Since the time t increases continuously, there is a point on the wave profile (5.4) and a time for which

$$t = -\frac{h_1}{F_1 p_M(X)}.$$

When this occurs, the curvature will become

$$-\frac{\cos(n_M X)}{\epsilon^2 n_M^2 \sin^3(n_M X)}$$

at that particular point. It follows at once from this result that there are points (near the crests and troughs of the wave profile) for which the curvature may become arbitrarily large at appropriate times. This shows that curvature singularities of the type seen in this paper are a natural consequence of fluid shear. Furthermore, it gives strong confirmation of the accuracy of our new algorithm in Section 4, which is able to predict such behaviour accurately.

The predictions of this asymptotic solution are shown in Figure 7, for the same parameter values as in Figure 4, and at the same two times $t = 1$ and $t = 6.8$. In Figure 7(a), the interface is presented at these two times, and is calculated from equation (5.4). It compares reasonably well with the numerically obtained interface in Figure 4(a), except that its amplitude is not subject to the same level of decay with time as in Figure 4(a). This decay was mostly caused, of course, by the inclusion of the Lanczos smoothing parameter, which had to be set at the rather high value $\sigma_L = 0.2$ so that solutions could be generated at the later time $t = 6.8$. As mentioned in the discussion of Figure 4, this does have a significant effect on the numerical solution, and is responsible for the decay in Figure 4(a). By contrast, there is no possible deterioration of the wave in Figure 7, because it has been assumed in this asymptotic approach that the flow remains horizontal, and the evolution of the wave is, therefore, purely the result of shear.

The curvature for this same case, computed from the asymptotic formula (5.6), is shown in Figure 7(b) at time $t = 6.8$. Here, although equation (5.6) predicts essentially infinite curvature at certain points, the result is shown only on the same vertical scale as in Figure 4(b) so as to facilitate comparison. There is clearly very good agreement between Figures 4(b) and 7(b), particularly with respect to the location and timing of the occurrences of the singularities, although the strength of the peaks in Figure 4(b) has deteriorated somewhat, again because of the inclusion of the Lanczos smoothing in that numerical solution. Nevertheless, the fact that the numerical scheme in Section 4 can calculate the curvature with such precision under such difficult circumstances represents a strong endorsement of this new algorithm.

https://doi.org/10.1017/S1446181115000085 Published online by Cambridge University Press

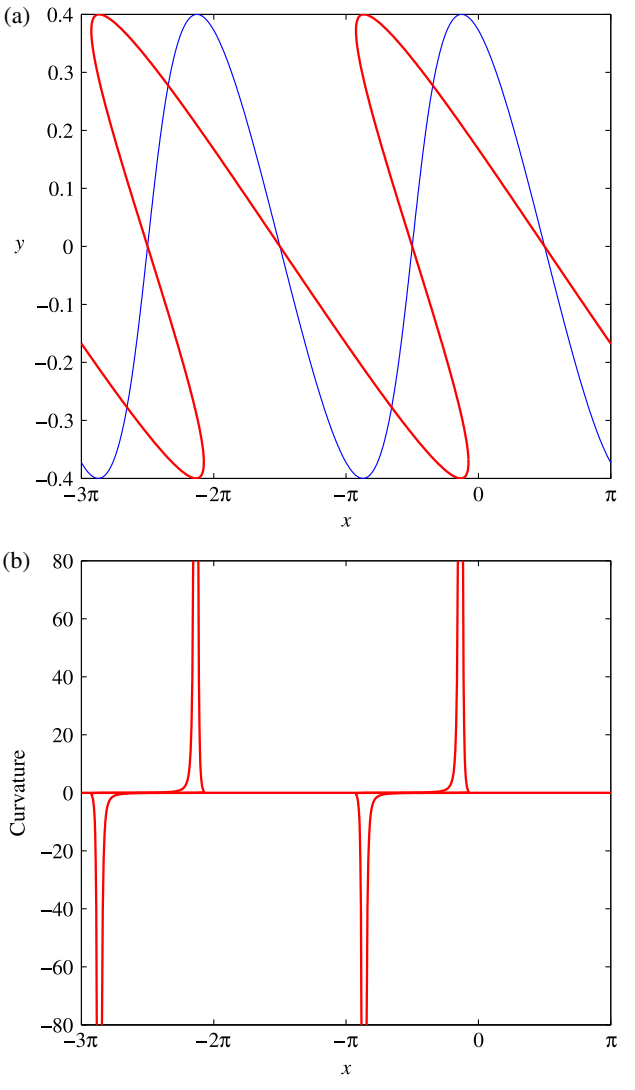

FIGURE 7. Nonlinear (a) interface shapes and (b) curvatures obtained for equal densities $D = 1$, with speeds $F_1 = 1$, $F_2 = -1$, viscosities $R_1 = R_2 = 1$ and fluid depths $h_1 = h_2 = 1$. The initial amplitude was $\epsilon = 0.4$, and results obtained from the asymptotic solution in Section 5.2 are shown at the two times $t = 1$ (blue online in part (a)) and $t = 6.8$ (thick; red online). (Colour available online.)

5.3. Results with two dissimilar fluids When the densities, viscosities and so on are no longer equal, no major qualitative change is observed in the solutions, although the wave profiles lose their symmetry about the neutral height $y = 0$. Two final examples are now given, to conclude this presentation of results. The first is displayed in Figure 8, for unequal densities $D = 0.97$ and unequal viscosities $R_1 = 1.2$,

https://doi.org/10.1017/S1446181115000085 Published online by Cambridge University Press

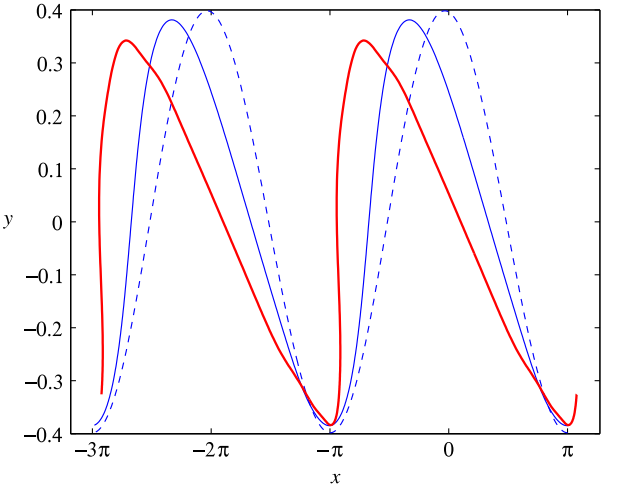

FIGURE 8. Nonlinear interface shapes obtained for density ratio $D = 0.97$, with speeds $F_1 = 1$, $F_2 = -1$ and viscosities $R_1 = 1.2$, $R_2 = 1$. Here, the lower fluid is deeper, and $h_1 = 2$, $h_2 = 1$. The surface tension is $\sigma = 0$ and the Lanczos smoothing parameter is set to $\sigma_L = 0.15$. The initial amplitude was $\epsilon = 0.4$. Results are shown at the three times $t = 0.2$ (dashed line), $t = 2$ (solid; blue line) and $t = 4.2$ (thick; red line). (Colour available online.)

$R_2 = 1$. Surface tension has been set to zero, but now the lower fluid 1 is twice the depth of the upper fluid 2, so that $h_1 = 2$, $h_2 = 1$. The two Froude numbers are $F_1 = 1$, $F_2 = -1$, and the linearized solution of Section 3 sets the growth rate in equation (3.14) to be $\lambda = -0.0019 \pm 0.2607i$. Thus, linearization predicts a weakly decaying wave, as a consequence of the viscosity and unequal densities.

The wave profile is shown at time $t = 0.2$, where it is drawn with a dashed line; it is almost indistinguishable from the cosinusoidal initial condition (4.26) with amplitude $\epsilon = 0.4$. The later profile at time $t = 2$ has leaned to the left, and the solution at the final time $t = 4.2$, drawn with a thicker line, is strongly distorted. In addition, it has clearly developed points of very high curvature and, with $N = 31$ Fourier coefficients and the value $\sigma_L = 0.15$ of the Lanczos smoothing parameter assumed here, this last solution is the largest time for which reliable solutions could be obtained. As discussed above, wave profiles can be computed for larger times, and be displaying considerably more distortion by increasing the Lanczos parameter σ_L, but that is not pursued further here. Nevertheless, overturning portions in the profile at time $t = 4.2$ are visible in the diagram. The waves are no longer symmetrical about the central line $y = 0$ and, in particular, the crests move strongly to the left while the troughs remain almost in the same location throughout the evolution of the solution.

The converse situation is shown in Figure 9, since in these diagrams the upper fluid is the deeper of the two with $h_1 = 1$ and $h_2 = 2$. The other parameters are the same as for Figure 8. At a first glance, the wave profile in Figure 9(a) looks something like that in Figure 8 but tipped upside down, since the crests are now narrower than the troughs.

https://doi.org/10.1017/S1446181115000085 Published online by Cambridge University Press

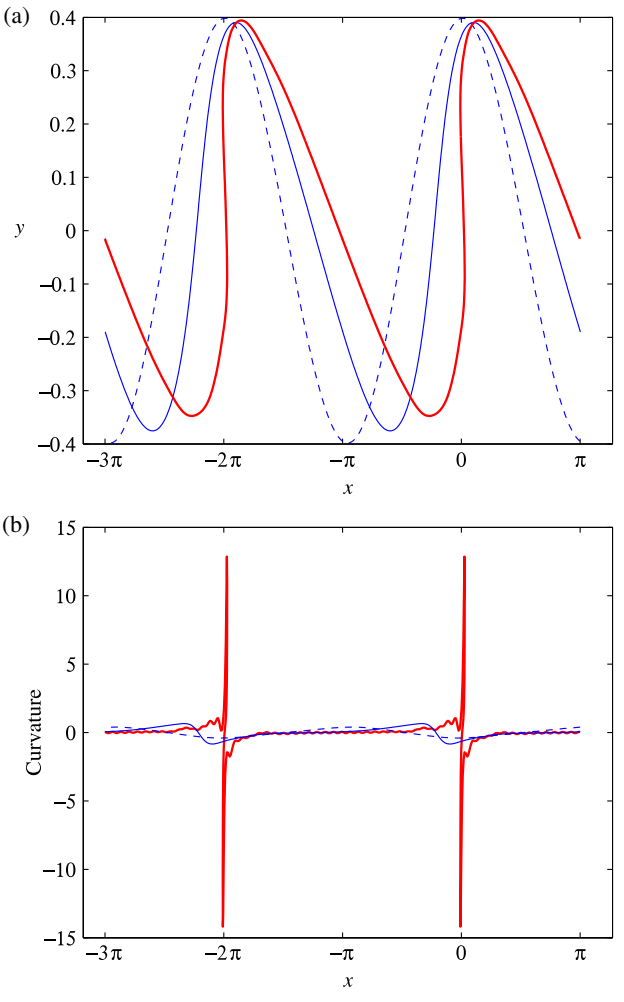

FIGURE 9. Nonlinear (a) interface shapes and (b) curvatures obtained for density ratio $D = 0.97$ with speeds $F_1 = 1$, $F_2 = -1$ and viscosities $R_1 = 1.2$, $R_2 = 1$. Here, the upper fluid is deeper, and $h_1 = 1$, $h_2 = 2$. The surface tension is $\sigma = 0$ and the Lanczos smoothing parameter is set to $\sigma_L = 0.15$. The initial amplitude was $\epsilon = 0.4$. Results are shown at the three times $t = 0.2$ (dashed line), $t = 2$ (solid; blue online) and $t = 3.6$ (thick; red online).

Solutions are again shown at times $t = 0.2$ (dashed line) and $t = 2$ (solid line), but now the algorithm with Lanczos parameter $\sigma_L = 0.15$ would not progress past time $t = 3.6$, and so this is the last time shown in Figure 9(a), drawn with a thicker solid line. In this case, the crests stay nearly in the same position as the solution develops and the troughs move to the right, although this again gives a narrow overhanging section in the wave profile at the last time $t = 3.6$.

https://doi.org/10.1017/S1446181115000085 Published online by Cambridge University Press

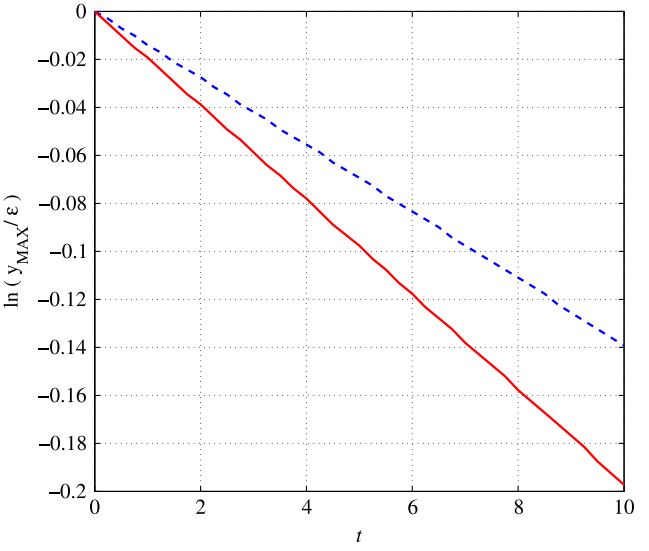

FIGURE 10. A comparison of the maximum wave height for the wave as a function of time, for the linearized solution (dashed; blue online) and the nonlinear solution (solid; red online) (Colour available online). The density ratio is $D = 0.8$, the speeds are $F_1 = 0.1$, $F_2 = -0.1$ and the viscosities are $R_1 = 1.2$, $R_2 = 1$. Here, the lower fluid is deeper, and $h_1 = 2$, $h_2 = 1$. The surface tension is $\sigma = 0$ and the Lanczos smoothing parameter is set to $\sigma_L = 0.1$. The initial amplitude was $\epsilon = 0.1$.

The curvatures for these three times are presented in Figure 9(b). At the earliest time $t = 0.2$, sketched with a dashed line, the curvature is closely approximated by the second derivative of the initial profile (4.26), as expected from the linearized solution, but by time $t = 2$ nonlinear effects are strongly in evidence, as the solution contains long almost flat sections interrupted by narrow S-shaped portions. At the last time $t = 3.6$, the curvature has developed large spikes at about $x = 0$, towards the top of the wave profile there. These curvature spikes are strongly reminiscent of the Moore curvature singularity encountered in purely inviscid Kelvin–Helmholtz flows [20], and they further indicate that the wave profile does indeed overturn slightly. As with Figure 4(a), solutions can be obtained in this case, too, at later times and exhibiting far stronger overturning fingers, by increasing the value of the Lanczos parameter σ_L, but that is not pursued further here.

A comparison of the maximum wave heights with time is given in Figure 10, for the linearized solution of Section 3 and the nonlinear case in Section 4. This figure is analogous to those presented by Pozrikidis [22], and it similarly shows the natural logarithm of the maximum wave height y_{MAX} divided by the initial maximum value ϵ. Here, the parameters are chosen to give a strong difference in the properties of the two fluids, so that the density ratio is $D = 0.8$, the fluid viscosities are $R_1 = 1.2$, $R_2 = 1$ and the depths are also dissimilar with $h_1 = 2$, $h_2 = 1$. A wave of smaller initial amplitude $\epsilon = 0.1$ has been chosen, and the focus is on the earlier times $0 < t < 10$. For this case, we found it necessary to set the Lanczos parameter $\sigma_L = 0.1$ in order

https://doi.org/10.1017/S1446181115000085 Published online by Cambridge University Press

to overcome the ill-conditioning of the problem. The linearized solution has a decay rate calculated from equation (3.14) to be $\Re\{\lambda\} = -0.0139$, and this is precisely the slope of the dashed line in Figure 10, as expected; its decay is the result of the fluid viscosities. The nonlinear result is shown with a solid line and, although its slope at $t = 0$ agrees well with the linearized value, it must be acknowledged again that the inclusion of the Lanczos parameter σ_L has a significant additional damping effect on the wave, as discussed previously. Consequently, the nonlinear curve soon develops a larger more negative slope, reflecting the influence of Lanczos damping. Very similar results to Figure 10 are produced for all the other cases studied in this investigation.

6. Boussinesq–Stokes approximation

In the Boussinesq approximation, it is assumed that the density ρ of the fluid is a smoothly varying function so that, necessarily, the true interface that is subject to conditions (2.5)–(2.8) is simply ignored. Instead, the density varies continuously from the value $\rho = 1$ at the lower wall $z = -h_1$ to $\rho = D$ at the upper wall $z = h_2$, in these dimensionless variables. The density is expressed in the form $\rho = 1 + \bar{\rho}$, and it is assumed that the perturbation variable $\bar{\rho}$ remains small. In the present application, $\bar{\rho} \to 0$ as $y \to -h_1$ and $\bar{\rho} \to -(1 - D)$ as $y \to h_2$, with a continuous but rapidly varying section in the region corresponding to the location of the interface. The governing equations are, therefore,

$$\nabla p = -(1 + \bar{\rho})\mathbf{j} + R\nabla^2\mathbf{q}, \tag{6.1}$$

replacing equations (2.3) and (2.4), along with the usual incompressibility condition (2.2). There is also a transport equation

$$\frac{\partial \bar{\rho}}{\partial t} + \mathbf{q} \cdot \nabla\bar{\rho} = K\nabla^2\bar{\rho} \tag{6.2}$$

for the density perturbation function $\bar{\rho}$, in which the constant K is a diffusion coefficient. Physically, it can be regarded as a Prandtl number, or in some circumstances as a thermal diffusion coefficient as discussed in Forbes [12].

The solution of the equations (6.1) and (6.2) is accomplished using the spectral representations

$$u(x, y, t) = \frac{1}{(h_2 + h_1)}[F_2(y + h_1) - F_1(y - h_2)] + \sum_{m=1}^{M}\sum_{n=1}^{N} b'_{mn}(y)[A_{mn}(t)\cos(nx) + B_{mn}(t)\sin(nx)], \tag{6.3}$$

$$v(x, y, t) = \sum_{m=1}^{M}\sum_{n=1}^{N} nb_{mn}(y)[A_{mn}(t)\sin(nx) - B_{mn}(t)\cos(nx)] \tag{6.4}$$

for the two velocity components. These may be derived from a streamfunction ψ, which is not given here in the interests of space, and they satisfy the incompressibility

https://doi.org/10.1017/S1446181115000085 Published online by Cambridge University Press

condition (2.2) identically. It follows, by taking the vector curl of the Boussinesq–Stokes momentum equation (6.1), that the density perturbation function $\bar{\rho}$ is related to the streamfunction ψ through a vorticity equation of the form

$$\frac{\partial \bar{\rho}}{\partial x} = -R\nabla^4\psi. \tag{6.5}$$

This results in the spectral representation

$$\frac{\partial \bar{\rho}}{\partial x} = -R\sum_{m=1}^{M}\sum_{n=1}^{N}[b_{mn}^{(4)}(y) - 2n^2 b_{mn}''(y) + n^4 b_{mn}(y)] \times [A_{mn}(t)\cos(nx) + B_{mn}(t)\sin(nx)]. \tag{6.6}$$

In this novel spectral solution of the approximate Boussinesq–Stokes model (6.1)–(6.2), we choose the basis functions $b_{mn}(y)$ to satisfy the fourth-order differential equation

$$b_{mn}^{(4)}(y) - 2n^2 b_{mn}''(y) + n^4 b_{mn}(y) = \sin\left(\frac{m\pi(y+h_1)}{h_2+h_1}\right) \tag{6.7}$$

along with the four boundary conditions

$$b_{mn}(-h_1) = 0, \quad b_{mn}(h_2) = 0,$$
$$b_{mn}'(-h_1) = 0, \quad b_{mn}'(h_2) = 0,$$

in order to obey the no-slip conditions at the two walls. After some algebra, this results in the choice

$$\begin{aligned} b_{mn}(y) = {} & \frac{(m\pi)/(h_2+h_1)}{C_{mn}^4[\sinh^2 n(h_2+h_1) - n^2(h_2+h_1)^2]} \\ & \times\{(y+h_1)\sinh n(y-h_2)[\sinh n(h_2+h_1) + \cos(m\pi)n(h_2+h_1)] \\ & - (y-h_2)\sinh n(y+h_1)[n(h_2+h_1) + \cos(m\pi)\sinh n(h_2+h_1)]\} \\ & + \frac{1}{C_{mn}^4}\sin\left(\frac{m\pi(y+h_1)}{h_2+h_1}\right), \end{aligned} \tag{6.8}$$

where auxiliary constants

$$C_{mn}^2 = n^2 + \left(\frac{m\pi}{h_2+h_1}\right)^2 \tag{6.9}$$

have been defined for convenience. In view of this choice (6.8), the appropriate representation for the density perturbation function is obtained from equation (6.6) to be

$$\begin{aligned} \bar{\rho}(x,y,t) = {} & -(1-D)\left(\frac{y+h_1}{h_2+h_1}\right) + \sum_{m=1}^{M} B_{m0}(t)\sin\left(\frac{m\pi(y+h_1)}{h_2+h_1}\right) \\ & - R\sum_{m=1}^{M}\sum_{n=1}^{N}\frac{1}{n}\sin\left(\frac{m\pi(y+h_1)}{h_2+h_1}\right)[A_{mn}(t)\sin(nx) - B_{mn}(t)\cos(nx)]. \end{aligned} \tag{6.10}$$

https://doi.org/10.1017/S1446181115000085 Published online by Cambridge University Press

The coefficients $A_{mn}(t)$ and $B_{mn}(t)$ in the representations (6.3)–(6.10) are obtained from the density-transport equation (6.2) after Fourier decomposition. This leads to the systems of ordinary differential equations

$$B'_{k0}(t) = -KB_{k0}(t)\left(\frac{k\pi}{h_2+h_1}\right)^2 - \frac{1}{\pi(h_2+h_1)}\int_{-h_1}^{h_2}\int_{-\pi}^{\pi}\left(u\frac{\partial\bar\rho}{\partial x}+v\frac{\partial\bar\rho}{\partial y}\right)\sin\left(\frac{k\pi(y+h_1)}{h_2+h_1}\right)dx\,dy, \quad k=1,2,\ldots,M, \tag{6.11}$$

and

$$A'_{k\ell}(t) = -KC_{k\ell}^2A_{k\ell}(t) + \frac{2\ell}{\pi(h_2+h_1)R}\int_{-h_1}^{h_2}\int_{-\pi}^{\pi}\left(u\frac{\partial\bar\rho}{\partial x}+v\frac{\partial\bar\rho}{\partial y}\right)\sin\left(\frac{k\pi(y+h_1)}{h_2+h_1}\right)\sin(\ell x)\,dx\,dy, \quad k=1,2,\ldots,M,\ \ell=1,2,\ldots,N. \tag{6.12}$$

The equations for the derivatives $B'_{k\ell}(t)$ are the same as for (6.12), except that every appearance of $A_{k\ell}$ is replaced by $B_{k\ell}$ and $\sin(\ell x)$ in the integrand is replaced with $-\cos(\ell x)$.

Initial conditions are chosen to be consistent with those adopted in the linearized solution of Section 3 and the corresponding nonlinear profile (4.26). Accordingly, the initial perturbation density function is taken to be

$$\bar\rho(x,y,0) = \begin{cases} 0 & \text{if } -h_1 < y < \epsilon\cos(n_Mx), \\ -(1-D) & \text{if } \epsilon\cos(n_Mx) < y < h_2. \end{cases} \tag{6.13}$$

This initial density profile (6.13) is similarly subject to Fourier decomposition, to yield starting values $B_{k0}(0)$, $A_{k\ell}(0)$ and $B_{k\ell}(0)$ for the differential equations (6.11) and (6.12). These involve certain integrals, which are evaluated using the Gaussian quadrature routine of von Winckel [28]. The quadratures in the differential equations (6.11) and (6.12) are evaluated in the same manner at each time step. Finally, this system of $M(2N+1)$ differential equations is integrated forward in time using the adaptive Runge–Kutta–Fehlberg routine *ode45* provided by *MATLAB*.

Figure 11 shows profiles of the density perturbation function $\bar\rho$ computed from the spectral representation (6.10) starting from the initial condition (6.13) with amplitude $\epsilon = 0.4$ at the first mode $n_M = 1$. In the upper portion of each diagram (blue online), the density function has the value $\bar\rho = -0.03$ and the lower portion (red online) represents $\bar\rho = 0$. The mottled appearance of this lower section is caused by very small amplitude waves resulting from Gibbs' phenomenon [18, p. 510], and is of no consequence. There is a narrow interfacial region, across which the density function changes rapidly but smoothly between these two values. The three diagrams show the development of the Boussinesq–Stokes solution at the three times $t = 10$, 20 and 30, and the interfacial zone forms a steepening front on the left-hand side, eventually overhanging at about

https://doi.org/10.1017/S1446181115000085 Published online by Cambridge University Press

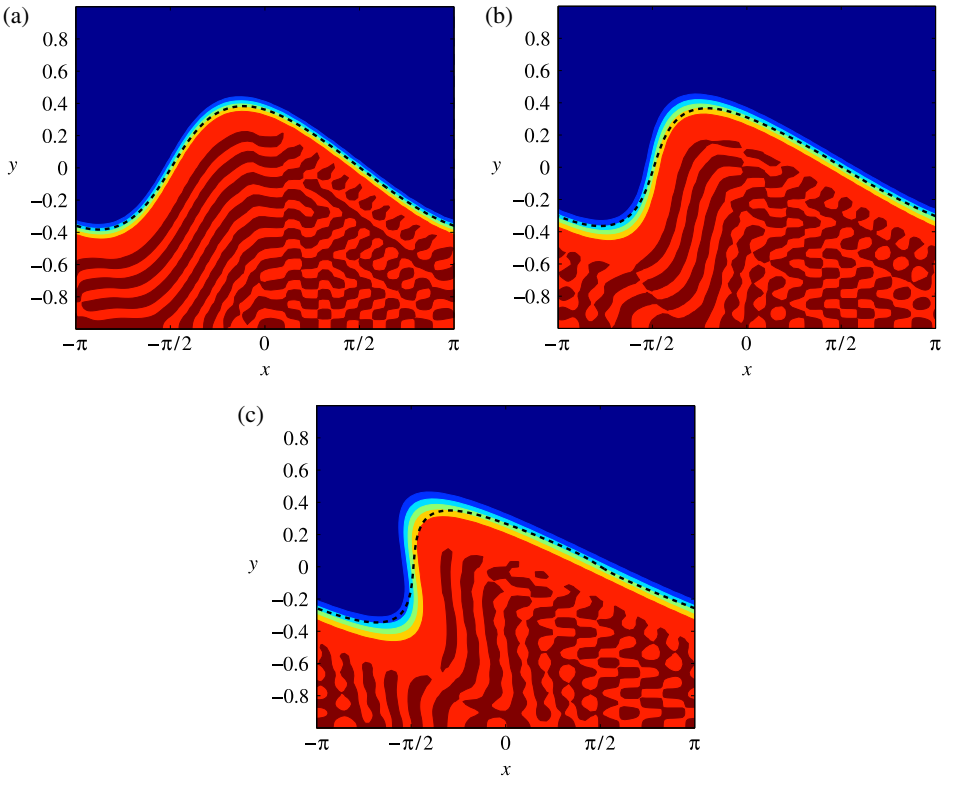

FIGURE 11. Density profiles computed using the Boussinesq–Stokes approximation, for times (a) $t = 10$, (b) $t = 20$ and (c) $t = 30$. The density ratio is $D = 0.97$, with speeds $F_1 = 0.1$, $F_2 = -0.1$ and viscosity parameter $R = 1$. The two fluid depths are equal, with $h_1 = h_2 = 1$, and the diffusion coefficient is $K = 10^{-4}$. The initial amplitude was $\epsilon = 0.4$. The heavy dashed line is the interface computed from the Stokes model of Section 4 with $R_1 = R_2 = 1$ and Lanczos smoothing parameter $\sigma_L = 0.15$. (Colour available online.)

time $t = 30$. The heavy dashed line in each of these three pictures is the location of the interface computed for the same parameter values from the representation (4.3) in Section 4. At the earliest time $t = 10$, it lies almost precisely in the midst of the interfacial zone predicted by the Boussinesq–Stokes approximation. As time progresses, however, the exact interface (4.3) is not as free to form overhanging portions as the simpler Boussinesq–Stokes approximation, but, instead, begins to develop regions of very high curvature. Consequently, the two sets of results differ slightly in the region of the front at later times. The Lanczos smoothing parameter was taken to be $\sigma_L = 0.15$ for the calculation of the interface, but checking confirmed that this had no significant effect on the interface profile at these three times shown.

For interest, the predictions of the Boussinesq–Stokes approximation at the much later time $t = 60$ are shown in Figure 12. Curvature singularities in the exact interface have prevented the solution of Section 4 from continuing to this late time, and so there

https://doi.org/10.1017/S1446181115000085 Published online by Cambridge University Press

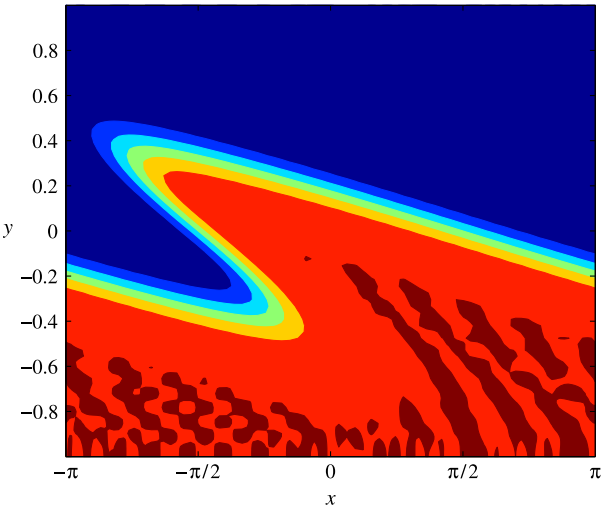

FIGURE 12. Density profile computed using the Boussinesq–Stokes approximation at time $t = 60$. The parameter values are the same as for Figure 11.

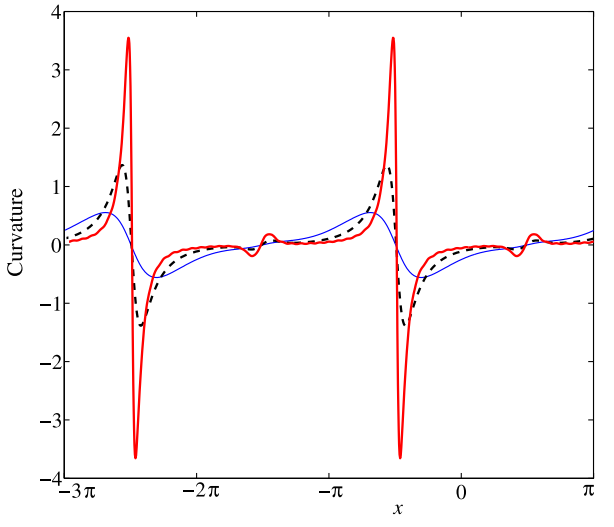

FIGURE 13. Curvatures for the three interfaces shown in Figure 11, at the times $t = 10$ (thin blue line), $t = 20$ (heavy black dashed line) and $t = 30$ (thick solid red line). (Colour available online.)

is no comparison possible between the two in Figure 12. The severely overhanging interface in Figure 12 is qualitatively similar to those presented by Pozrikidis [22].

The curvatures of the three interfacial profiles sketched with heavy dashed lines in Figure 11 are shown in Figure 13 at the same three times, $t = 10$, 20 and 30. Again it is found that at certain points along the interfacial profile, the curvature develops

https://doi.org/10.1017/S1446181115000085 Published online by Cambridge University Press

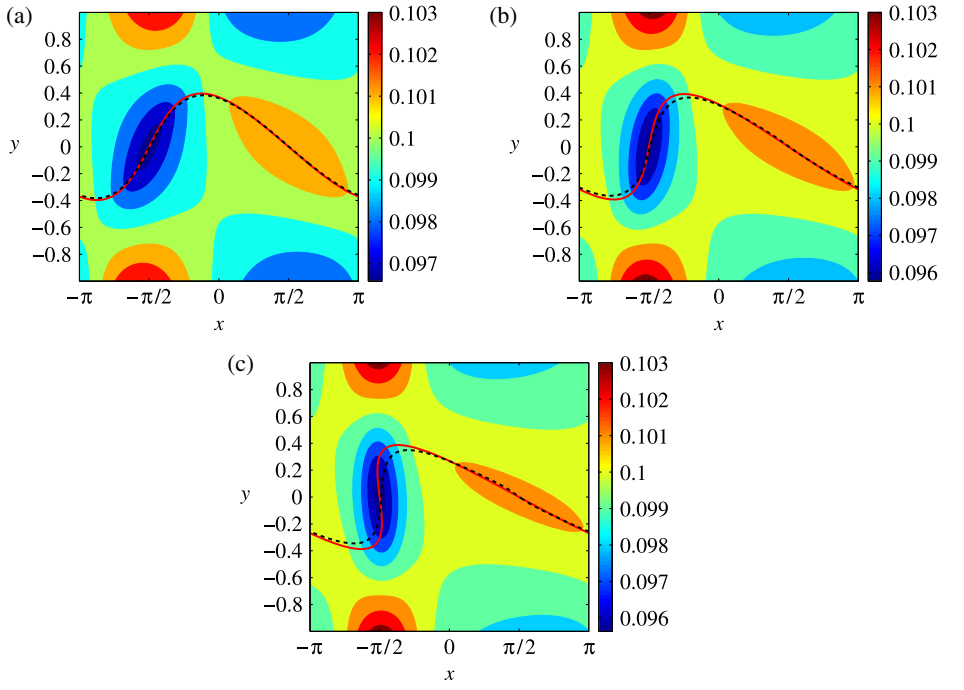

FIGURE 14. Vorticity profiles computed using the Boussinesq–Stokes approximation, for times (a) $t = 10$, (b) $t = 20$ and (c) $t = 30$. The density ratio is $D = 0.97$, with speeds $F_1 = 0.1$, $F_2 = -0.1$ and viscosity parameter $R = 1$. The two fluid depths are equal, with $h_1 = h_2 = 1$, and the diffusion coefficient is $K = 10^{-4}$. The initial amplitude was $\epsilon = 0.4$. The heavy dashed line is the interface computed from the Stokes model of Section 4. The heavy (red) solid line is the density contour $\bar{\rho} = -0.015$ that most nearly represents the interface location for the Boussinesq–Stokes approximation. (Colour available online.)

large spikes as encountered previously in Figures 2, 4 and 9. Evidently, the curvature becomes singular at some finite time, analogous to the situation described by Moore [20] in the purely inviscid Kelvin–Helmholtz flow, and these singularities ultimately render the Stokes theory invalid beyond that critical time.

To conclude this comparison with Boussinesq–Stokes theory, it is of interest to consider the vorticity function $\zeta = \partial v/\partial x - \partial u/\partial y$. This is calculated in spectral form from the representations (6.3) and (6.4), and is illustrated in Figure 14 for the same three times, $t = 10$, 20 and 30 and the same parameter values as in Figure 11. In these three diagrams, contours of the function ζ are shown and, in each case, there are two additional curves overlaid on the picture. One of these is a thick solid line, and represents the location of the density contour $\bar{\rho} = -(D-1)/2 = -0.015$. This is the median value of the perturbation density function, and so serves as a proxy for the location of the interface, as calculated by the Boussinesq–Stokes approximation. The other curve is indicated with a heavy dashed line and is the exact interface location calculated from the Stokes model in Section 4; this is the same set of curves as

https://doi.org/10.1017/S1446181115000085 Published online by Cambridge University Press

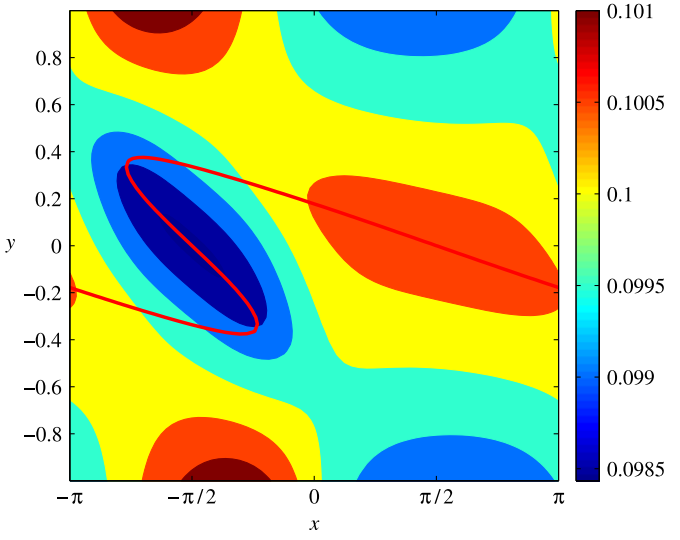

FIGURE 15. Vorticity profile computed using the Boussinesq–Stokes approximation at time $t = 60$. The parameter values are the same as for Figure 14. The heavy (red) solid line is the density contour $\bar{\rho} = -0.015$ that most closely represents the interface location for the Boussinesq–Stokes approximation. (Colour available online.)

plotted in Figure 11. As seen previously, there is a very close agreement between the two curves at early times, but they differ near the developing front by the later time $t = 30$. Most noticeably, a strong patch of vorticity is predicted by the approximate Boussinesq–Stokes theory to develop near the location of the front, and this is evident in Figure 14(a)–(c). It is ultimately responsible for the overturning of the front in this theory; by contrast, the exact interface is ultimately limited by the formation of curvature singularities, and these have been illustrated in Figure 13.

As a final point of interest, the vorticity contours computed from the Boussinesq–Stokes theory at the later time $t = 60$ are shown in Figure 15. Additionally, the median density contour $\bar{\rho} = -0.015$ has been overlaid on the figure, as an indication of the shape of the interfacial zone, and has been extracted from the results shown in Figure 12. The strong patch of vorticity that accompanies the overturning interface in this approximation is still visible, although its intensity has dissipated, relative to the earlier times shown in Figure 14.

7. Discussion and conclusion

This paper has presented a novel spectral method for computing the large-amplitude disturbances to an interface between two very viscous fluids governed by the Stokes-flow approximation. In addition, the full linearized solution has been developed. The original intention here was to devise a computational method that represented a straightforward extension of the *extended* approach of Forbes et al. [13] to new

https://doi.org/10.1017/S1446181115000085 Published online by Cambridge University Press

situations involving the Stokes flow. That approach made use of the arclength method, as in Section 4, and then converted all the interfacial boundary conditions into ordinary differential equations for the Fourier coefficients by an exact differentiation of the Fourier expressions at the interface with respect to time. While this philosophy is highly successful for purely inviscid fluids in which Bernoulli's equation allows the pressure at the interface to be calculated directly from the fluid velocity, in the present viscous application it turns out to be significantly less successful. Not only is it complicated to implement, but, more importantly, it gives rise to a poorly conditioned numerical problem.

Accordingly, the new algorithm of Section 4 derives ordinary differential equations for the Fourier coefficients describing the wave profile as in the inviscid method of Forbes et al. [13]. However, it then solves purely algebraic equations for the Fourier coefficients of the representations for the streamfunctions and pressures in each fluid. The method is fast and accurate, and allows sensitive quantities, such as the curvature of the interface, to be calculated extremely accurately. Possibly, the weakest feature of the method is that it uses simple Euler time stepping to advance the ordinary differential equations in time. This could be replaced with a more sophisticated quadrature, but at a highly increased computational cost, possibly involving iteration at each time step. Here, we found it easier to maintain accuracy simply by using a large number of time steps, and this has been implemented in a scheme that involves two embedded loops.

Our numerical results give strong support to the suggestion that even for Stokes flow of highly viscous fluids, the interface may develop singularities within finite time. This is already known to be possible in other geometries, and Siegel [24] has shown that bubbles in straining viscous flow become elongated, and may eventually form cusp singularities at their pointed ends within finite time. Similarly, Eggers and Villermaux [9] surveyed singularities that may form in the pinch-off of fluid jets. However, the present work also suggests that *planar* singularities closely analogous to Moore's curvature singularity [20] may occur for periodic waves, and in about the same location as for the inviscid Kelvin–Helmholtz instability, namely, at the point where the linearized approximation has an inflection point in the profile.

Forbes [11] demonstrated numerically that the role of viscosity is to replace Moore's curvature singularity [20] at the interface of inviscid fluids with a small region of high vorticity, giving rise in time to overturning of the interface. However, the results of the present paper may also suggest that viscosity alone may not be responsible for creating the small patch of high vorticity, but, instead, viscosity combined with inertial terms and a finite-thickness interfacial zone may account for this effect. Indeed, in the approximate Boussinesq–Stokes theory developed in Section 6, it has been demonstrated that replacing the exact interface with a smooth interfacial zone permits a strongly overhanging portion to develop in the wave profile. In the exact formulation of Section 4, it has also been shown that introducing a small degree of smoothing in the Fourier domain, using the Lanczos philosophy in which an interface location at a point is replaced by its average over a small region centred at

this point, can allow the evolution of the interface to continue past the critical time of singularity formation and permit the formation of overhanging fingers. While Lanczos smoothing does not appreciably alter the solution for early times, it must be admitted that it does change the interface at later times, and in that respect it is similar to the *vortex blob* methods introduced by Krasny [17] and others, designed specifically to permit inviscid interfaces to continue evolving after the critical time, and to overturn. It is even possible that the boundary-integral approach of Pozrikidis [22], for example, may implicitly encode a similar damping mechanism, as the exact integrals along the interface are eventually discretized in the final algorithm.

A new asymptotic theory has been presented in Section 5.2, and it shows how the curvature singularities encountered in this paper are the result of shearing in the flow. Thus, it seems possible that curvature singularities may be a feature of time-dependent free-surface flows of both inviscid fluids [20] and highly viscous fluids. Indeed, Barnea and Taitel [3] provided a detailed discussion of the highly nonintuitive fact that very viscous Kelvin–Helmholtz flows behave surprisingly similarly to completely inviscid ones. Crucially, the Stokes approximation (2.1) ignores the nonlinear convection terms in the full Navier–Stokes system, and these may also have a key role in suppressing curvature singularities at the interface.

Acknowledgements

This work has been carried out in connection with Australian Research Council discovery grant DP140100094. Comments from four reviewers are gratefully acknowledged.

References

[1] M. Abramowitz and I. A. Stegun (eds), *Handbook of mathematical functions* (Dover, New York, 1972).

[2] G. R. Baker and L. D. Pham, "A comparison of blob-methods for vortex sheet roll-up", *J. Fluid Mech.* **547** (2006) 297–316; doi:10.1017/S0022112005007305.

[3] D. Barnea and Y. Taitel, "Kelvin–Helmholtz stability criteria for stratified flow: viscous versus non-viscous (inviscid) approaches", *Int. J. Multiphase Flow* **19** (1993) 639–649; doi:10.1016/0301-9322(93)90092-9.

[4] G. K. Batchelor, *An introduction to fluid dynamics* (Cambridge University Press, Cambridge, 1967).

[5] S. Chandrasekhar, *Hydrodynamic and hydromagnetic stability* (Dover, New York, 1981).

[6] M. J. Chen and L. K. Forbes, "Accurate methods for computing inviscid and viscous Kelvin–Helmholtz instability", *J. Comput. Phys.* **230** (2011) 1499–1515; doi:10.1016/j.jcp.2010.11.017.

[7] S. J. Cowley, G. R. Baker and S. Tanveer, "On the formation of Moore curvature singularities in vortex sheets", *J. Fluid Mech.* **378** (1999) 233–267; doi:10.1017/S0022112098003334.

[8] P. G. Drazin and W. H. Reid, *Hydrodynamic stability*, 2nd edn (Cambridge University Press, Cambridge, 2004).

[9] J. Eggers and E. Villermaux, "Physics of liquid jets", *Rep. Progr. Phys.* **71** (2008) 1–79; doi:10.1088/0034-4885/71/3/036601.

[10] O. Faltinsen and A. Timokha, "An adaptive multimodal approach to nonlinear sloshing in a rectangular tank", *J. Fluid Mech.* **432** (2001) 167–200; http://journals.cambridge.org/action/displayAbstract?fromPage=online&aid=78569.

[11] L. K. Forbes, "The Rayleigh–Taylor instability for inviscid and viscous fluids", *J. Engrg. Math.* **65** (2009) 273–290; doi:10.1007/s10665-009-9288-9.
[12] L. K. Forbes, "How strain and spin may make a star bi-polar", *J. Fluid Mech.* **746** (2014) 332–367; doi:10.1017/jfm.2014.130.
[13] L. K. Forbes, M. J. Chen and C. E. Trenham, "Computing unstable periodic waves at the interface of two inviscid fluids in uniform vertical flow", *J. Comput. Phys.* **221** (2007) 269–287; doi:10.1016/j.jcp.2006.06.010.
[14] L. K. Forbes and J. M. Cosgrove, "A line vortex in a two-fluid system", *J. Engrg. Math.* **84** (2014) 181–199; doi:10.1007/s10665-012-9606-5.
[15] R. W. Hamming, *Numerical methods for scientists and engineers* (McGraw-Hill, New York, 1973).
[16] D. E. Horsley and L. K. Forbes, "A spectral method for Faraday waves in rectangular tanks", *J. Engrg. Math.* **79** (2013) 13–35; doi:10.1007/s10665-012-9562-0.
[17] R. Krasny, "Desingularization of periodic vortex sheet roll-up", *J. Comput. Phys.* **65** (1986) 292–313; doi:10.1016/0021-9991(86)90210-X.
[18] E. Kreyszig, *Advanced engineering mathematics*, 9th edn (Wiley, New York, 2006).
[19] J. Li, Y. Y. Renardy and M. Renardy, "A numerical study of periodic disturbances on two-layer Couette flow", *Phys. Fluids* **10** (1998) 3056–3071; doi:10.1063/1.869834.
[20] D. W. Moore, "Spontaneous appearance of a singularity in the shape of an evolving vortex sheet", *Proc. R. Soc. Lond. A* **365** (1979) 105–119; doi:10.1098/rspa.1979.0009.
[21] H. Ockendon and J. R. Ockendon, *Viscous flow* (Cambridge University Press, Cambridge, 1995).
[22] C. Pozrikidis, "Instability of two-layer creeping flow in a channel with parallel-sided walls", *J. Fluid Mech.* **351** (1997) 139–165; doi:10.1017/S0022112097007052.
[23] M. S. Shadloo and M. Yildiz, "Numerical modeling of Kelvin–Helmholtz instability using smoothed particle hydrodynamics", *Internat. J. Numer. Methods Engrg.* **87** (2011) 988–1006; doi:10.1002/nme.3149.
[24] M. Siegel, "Cusp formation for time-evolving bubbles in two-dimensional Stokes flow", *J. Fluid Mech.* **412** (2000) 227–257; doi:10.1017/S002211200000834X.
[25] W. Tauber, S. O. Unverdi and G. Tryggvason, "The nonlinear behavior of a sheared immiscible fluid interface", *Phys. Fluids* **14** (2002) 2871–2885; doi:10.1063/1.1485763.
[26] G. Tryggvason, W. J. A. Dahm and K. Sbeih, "Fine structure of vortex sheet rollup by viscous and inviscid simulation", *J. Fluids Engrg.* **113** (1991) 31–36; doi:10.1115/1.2926492.
[27] M. Van Dyke, *An album of fluid motion* (Parabolic Press, Stanford, CA, 1982).
[28] G. von Winckel, *lgwt.m*, at: MATLAB file exchange website (2004), http://www.mathworks.com/matlabcentral/fileexchange/loadFile.do?objectId=4540&objectType=file.